

---

# Entropy Stable $h/p$ -Nonconforming Discretization with the Summation-by-Parts Property for the Compressible Euler and Navier–Stokes Equations

David C. Del Rey Fernández · Mark H. Carpenter · Lisandro Dalcin · Stefano Zampini · Matteo Parsani

Received: date / Accepted: date

**Abstract** In this paper, the entropy conservative/stable algorithms presented by Del Rey Fernández and coauthors [18,16,17] for the compressible Euler and Navier–Stokes equations on nonconforming  $p$ -refined/coarsened curvilinear grids is extended to  $h/p$  refinement/coarsening. The main difficulty in developing nonconforming algorithms is the construction of appropriate coupling procedures across nonconforming interfaces. Here, a computationally simple and efficient approach based upon using decoupled interpolation operators is utilized. The resulting scheme is entropy conservative/stable and element-wise conservative. Numerical simulations of the isentropic vortex and viscous shock propagation confirm the entropy conservation/stability and accuracy properties of the method (achieving  $\sim p + 1$  convergence) which are comparable to those of the original conforming scheme [4,35]. Simulations of the Taylor–Green vortex at  $Re = 1,600$  and turbulent flow past a sphere at  $Re = 2,000$  show the robustness and stability properties of the overall spatial discretization for unstructured grids. Finally, to demonstrate the entropy conservation property of a fully-discrete explicit entropy stable algorithm with  $h/p$  refinement/coarsening, we present the time evolution of the entropy function obtained by simulating the propagation of the isentropic vortex using a relaxation Runge–Kutta scheme.

---

David C. Del Rey Fernández  
National Institute of Aerospace and Computational AeroSciences Branch, NASA Langley Research Center, Hampton, VA, United States  
E-mail: dcdelrey@gmail.com

Mark H. Carpenter  
NASA Langley Research Center, Hampton, VA, United States E-mail:  
mark.h.carpenter@nasa.gov

Lisandro Dalcin, Stefano Zampini, Matteo Parsani  
King Abdullah University of Science and Technology (KAUST), Computer Electrical and Mathematical Science and Engineering Division (CEMSE), Extreme Computing Research Center (ECRC), Thuwal, Saudi Arabia E-mail: dalcinl@gmail.com, stefano.zampini@kaust.edu.sa, matteo.parsani@kaust.edu.sa

**Keywords** Nonconforming interfaces ·  $h/p$  adaptation · Nonlinear entropy stability · Summation-by-parts · Simultaneous-approximation-terms · High-order accurate discretizations · Curved elements · Unstructured grid

## 1 Introduction

This paper is the final installment in a set aimed at developing arbitrarily high-order, entropy stable,  $h/p$ -nonconforming schemes on curvilinear coordinates for the compressible Euler and Navier–Stokes equations [27, 18, 16, 17]. The efficient use of exascale concurrency on next generation hardware motivates the search for algorithms that are accurate and robust. Moreover, essential to efficiency is the ability to optimally use degrees of freedom through  $h$ -,  $p$ -, and  $r$ -refinement/coarsening and communication hiding through dense compute kernels. High order methods are natural candidates for next generation hardware because they are accurate and their ratio of communications to local computations is usually small. However, they have historically been limited by robustness issues, which is even more important as problem size and physics complexity increases.

When numerically solving partial differential equations (PDEs) it is imperative to find a bound on the growth rate of the solution, otherwise the possibility exists that the solution could grow arbitrarily fast. This upper bound can be established by ensuring that a numerical method is stable. For linear variable coefficient problems in arbitrary dimensions, a general and systematic approach to ensure stability is the energy method because it can be applied to the continuous as well as the semi-discrete model. The energy method becomes extremely powerful when it is used in combination with the summation-by-parts (SBP) framework [20, 45] since it allows for the construction of provably stable schemes of any order. SBP operators can be viewed as strong or weak form differentiation matrices that mimic integration-by-parts (IBP) and are endowed with a telescoping property, critical for provable stability. Via this property, SBP schemes (augmented with appropriate interface coupling procedures, e.g., simultaneous approximation terms (SATs) [6, 7, 32, 33, 8, 46, 36, 37]) reproduce, in a one-to-one manner, continuous stability proofs. Therefore they provide a road map for the development of provably stable semi-discrete or fully discrete algorithms (see, for instance, [38, 26]).

For nonlinear problems a general and systematic approach for establishing stability has yet to be found. Nevertheless, for a certain class of PDEs progress has been made. For conservation laws, Tadmor [47] constructed entropy conservative/stable low-order finite volume schemes that achieve entropy conservation by using two-point flux functions. When contracted with entropy variables, these schemes telescope the entropy flux. Entropy stability is then achieved by adding appropriate dissipation. For a review of these ideas see, for instance, Tadmor [48].

Tadmor’s approach was extended to finite domains and arbitrary high order finite difference WENO schemes in the work of Fisher and coauthors who combined the SBP framework with Tadmor’s two-point flux functions, resulting in entropy stable semi-discrete schemes [23, 25, 24]. This approach inherits all of the mechanics of linear SBP schemes for the imposition of boundary conditions and inter-element coupling and gives a systematic methodology for discretizing problems on complex domains; see, for instance, [4, 36, 37, 54, 35, 28, 55, 53, 21, 52, 12, 11, 26, 19] and the reference therein. An alternative method applicable to the com-

compressible Euler equations [34, 56, 39, 40], uses specially chosen entropy functions that result in a homogeneity property on the compressible Euler fluxes. Via this property, the Euler fluxes are split such that when contracted with the entropy variables, stability estimates result that are analogous in form to energy estimates obtained for linear PDEs.

The objective of this paper is the extension of entropy stable  $p$ -nonconforming algorithm presented in Del Rey Fernández *et al.* [18, 16, 17] for the compressible Euler and Navier–Stokes equations in curvilinear coordinates to arbitrary  $h/p$ -refinement/coarsening. The novel contributions of this paper are summarized as follows:

- A general and simple entropy conservative/stable nonconforming algorithm is proposed in curvilinear coordinates for the compressible Euler and Navier–Stokes equations that
  - Enables a simple extension of the algorithm in [18, 16, 17] that uses the same type of interface SAT and therefore allows code re-utilization
  - Results in the solution of the discrete geometric conservation laws (GCL) that is local to each element
  - Applies the metric approximation approach of Crean *et al.* [12] to arbitrary  $h/p$ -nonconforming elements
  - Ensures free-stream preservation by satisfying the discrete GCL conditions
  - Is element-wise conservative
- Numerical evidence is provided to demonstrate that the scheme retains the stability and accuracy properties of the conforming base scheme [4, 35]

The paper is organized as follows. The notation is summarized in Section 2. In Section 3 the  $h/p$  nonconforming algorithm is detailed in the context of the linear convection-diffusion equation. The required nonlinear mechanic necessary to extend the nonconforming algorithm to the compressible Navier–Stokes equations is described in the simple context of the Burgers’ equation in Section 4. Section 5 details the extension of the nonconforming algorithm to the compressible Navier–Stokes equations. The addition of interface dissipation that retains the provable properties of the base algorithm is discussed in Section 6. Numerical experiments are detailed in Section 7 while conclusions are drawn in Section 8.

## 2 Notation and definitions

The notation used herein is identical to that in [18, 16, 17]; readers familiar with the notation can skip to Section 3. PDEs are discretized on cubes having Cartesian computational coordinates denoted by the triple  $(\xi_1, \xi_2, \xi_3)$ , where the physical coordinates are denoted by the triple  $(x_1, x_2, x_3)$ . Vectors are represented by lowercase bold font, for example  $\mathbf{u}$ , while matrices are represented using sans-serif font, for example,  $\mathbf{B}$ . Continuous functions on a space-time domain are denoted by capital letters in script font. For example,

$$\mathcal{U}(\xi_1, \xi_2, \xi_3, t) \in L^2([\alpha_1, \beta_1] \times [\alpha_2, \beta_2] \times [\alpha_3, \beta_3] \times [0, T])$$

represents a square integrable function, where  $t$  is the temporal coordinate. The restriction of such functions onto a set of mesh nodes is denoted by lower case bold

font. For example, the restriction of  $\mathcal{U}$  onto a grid of  $N_1 \times N_2 \times N_3$  nodes is given by the vector

$$\mathbf{u} = \left[ \mathcal{U}(\boldsymbol{\xi}^{(1)}, t), \dots, \mathcal{U}(\boldsymbol{\xi}^{(N)}, t) \right]^T,$$

where,  $N$  is the total number of nodes ( $N \equiv N_1 N_2 N_3$ ) square brackets ( $[]$ ) are used to delineate vectors and matrices as well as ranges for variables (the context will make clear which meaning is being used). Moreover,  $\boldsymbol{\xi}$  is a vector of vectors constructed from the three vectors  $\boldsymbol{\xi}_1$ ,  $\boldsymbol{\xi}_2$ , and  $\boldsymbol{\xi}_3$ , which are vectors of size  $N_1$ ,  $N_2$ , and  $N_3$  and contain the coordinates of the mesh in the three computational directions, respectively. Finally,  $\boldsymbol{\xi}$  is constructed as

$$\boldsymbol{\xi}(3(i-1) + 1 : 3i) \equiv \boldsymbol{\xi}^{(i)} \equiv [\boldsymbol{\xi}_1(i), \boldsymbol{\xi}_2(i), \boldsymbol{\xi}_3(i)]^T,$$

where the notation  $\mathbf{u}(i)$  means the  $i^{\text{th}}$  entry of the vector  $\mathbf{u}$  and  $\mathbf{u}(i:j)$  is the sub-vector constructed from  $\mathbf{u}$  using the  $i^{\text{th}}$  through  $j^{\text{th}}$  entries (i.e., Matlab notation is used).

Oftentimes, monomials are discussed and the following notation is used:

$$\boldsymbol{\xi}_l^j \equiv \left[ (\boldsymbol{\xi}_l(1))^j, \dots, (\boldsymbol{\xi}_l(N_l))^j \right]^T,$$

and the convention that  $\boldsymbol{\xi}_l^j = \mathbf{0}$  for  $j < 0$  is used.

Herein, one-dimensional SBP operators are used to discretize derivatives. The definition of a one-dimensional SBP operator in the  $\xi_l$  direction,  $l = 1, 2, 3$ , is [15, 20, 45]

**Definition 1 Summation-by-parts operator for the first derivative:** A matrix operator with constant coefficients,  $\mathbf{D}_{\xi_l}^{(1D)} \in \mathbb{R}^{N_l \times N_l}$ , is an SBP operator of degree  $p$  approximating the derivative  $\frac{\partial}{\partial \xi_l}$  on the domain  $\xi_l \in [\alpha_l, \beta_l]$  with nodal distribution  $\boldsymbol{\xi}_l$  having  $N_l$  nodes, if

1.  $\mathbf{D}_{\xi_l}^{(1D)} \boldsymbol{\xi}_l^j = j \boldsymbol{\xi}_l^{j-1}$ ,  $j = 0, 1, \dots, p$ ;
2.  $\mathbf{D}_{\xi_l}^{(1D)} \equiv \left( \mathbf{P}_{\xi_l}^{(1D)} \right)^{-1} \mathbf{Q}_{\xi_l}^{(1D)}$ , where the norm matrix,  $\mathbf{P}_{\xi_l}^{(1D)}$ , is symmetric positive definite;
3.  $\mathbf{Q}_{\xi_l}^{(1D)} \equiv \left( \mathbf{S}_{\xi_l}^{(1D)} + \frac{1}{2} \mathbf{E}_{\xi_l}^{(1D)} \right)$ ,  $\mathbf{S}_{\xi_l}^{(1D)} = - \left( \mathbf{S}_{\xi_l}^{(1D)} \right)^T$ ,  $\mathbf{E}_{\xi_l}^{(1D)} = \left( \mathbf{E}_{\xi_l}^{(1D)} \right)^T$ ,  $\mathbf{E}_{\xi_l}^{(1D)} = \text{diag}(-1, 0, \dots, 0, 1) = \mathbf{e}_{N_l} \mathbf{e}_{N_l}^T - \mathbf{e}_1 \mathbf{e}_1^T$ ,  $\mathbf{e}_1 \equiv [1, 0, \dots, 0]^T$ , and  $\mathbf{e}_{N_l} \equiv [0, 0, \dots, 1]^T$ .

Thus, a degree  $p$  SBP operator is one that differentiates exactly monomials up to degree  $p$ .

In this work, one-dimensional SBP operators are extended to multiple dimensions using tensor products ( $\otimes$ ). The tensor product between the matrices  $\mathbf{A}$  and  $\mathbf{B}$  is given as  $\mathbf{A} \otimes \mathbf{B}$ . When referencing individual entries in a matrix the notation  $\mathbf{A}(i, j)$  is used, which means the  $i^{\text{th}}$   $j^{\text{th}}$  entry in the matrix  $\mathbf{A}$ .

The focus in this paper is exclusively on diagonal-norm SBP operators. Moreover, the same one-dimensional SBP operator are used in each direction, each operating on  $N$  nodes. Specifically, diagonal-norm SBP operators constructed on the Legendre–Gauss–Lobatto (LGL) nodes are used, i.e., a discontinuous Galerkin collocated spectral element approach is utilized.

The physical domain  $\Omega \subset \mathbb{R}^3$ , with boundary  $\Gamma \equiv \partial\Omega$  is partitioned into  $K$  non-overlapping hexahedral elements. The domain of the  $\kappa^{\text{th}}$  element is denoted

by  $\Omega_\kappa$  and has boundary  $\partial\Omega_\kappa$ . Numerically, PDEs are solved in computational coordinates, where each  $\Omega_\kappa$  is locally transformed to  $\hat{\Omega}_\kappa$ , with boundary  $\hat{\Gamma} \equiv \partial\hat{\Omega}_\kappa$ , under the following assumption:

**Assumption 1** *Each element in physical space is transformed using a local and invertible curvilinear coordinate transformation that is compatible at shared interfaces, meaning that points in computational space on either side of a shared interface mapped to the same physical location and therefore map back to the analogous location in computational space; this is the standard assumption that the curvilinear coordinate transformation is water tight.*

### 3 An $h/p$ -nonconforming algorithm: Linear convection-diffusion equation

In this paper, the focus is on curvilinearly mapped elements with interfaces that 1) are conforming but have nonconforming nodal distributions, such as would arise in  $p$ -refinement, 2) elements that have nonconforming faces, such as would arise in  $h$ -refinement, and 3) arbitrary combinations of 1) and 2). The development of entropy stable  $h/p$ -refinement algorithm for the compressible Euler equations on Cartesian grids is detailed in [27]. The extension to curvilinear coordinates and  $p$ -refinement for the compressible Euler and Navier–Stokes equations is detailed in the series of papers [18, 17, 16], where an interface coupling technique is introduced that maintains, accuracy, discrete entropy conservation/stability, element-wise conservation and requires only local solves to approximate metric terms. Herein, the algorithm in [18, 17, 16] is extended to allow for arbitrary  $h/p$ -refinement on unstructured grids for the compressible Euler and Navier–Stokes equations.

#### 3.1 Continuous and semi-discrete analysis

A number of key technical difficulties that arise in developing a stable and conservative nonconforming discretization for the compressible Navier–Stokes equations are already present in the more simple context of the linear convection-diffusion equation. As a result, the proposed interface coupling procedure for both the inviscid and viscous terms are first presented for this simple linear scalar equation. In Cartesian coordinates, the linear convection-diffusion equation reads

$$\frac{\partial \mathcal{U}}{\partial t} + \sum_{m=1}^3 \frac{\partial (a_m \mathcal{U})}{\partial x_m} = \sum_{m=1}^3 \frac{\partial^2 (b_m \mathcal{U})}{\partial x_m^2}, \quad (1)$$

where  $(a_m \mathcal{U})$  and  $\frac{\partial (b_m \mathcal{U})}{\partial x_m}$  are the inviscid and viscous fluxes, respectively. The symbols  $a_m$  correspond to the constant components of the convection speed whereas  $b_m$  are the positive and constant diffusion coefficients. The stability of (1) can be determined via the energy method, which proceeds by multiplying (1) by the solution,  $(\mathcal{U})$ , and after using the product rule yields

$$\frac{1}{2} \frac{\partial \mathcal{U}^2}{\partial t} + \frac{1}{2} \sum_{m=1}^3 \frac{\partial (a_m \mathcal{U}^2)}{\partial x_m} = \sum_{m=1}^3 \left\{ \frac{\partial}{\partial x_m} \left( \mathcal{U} \frac{\partial (b_m \mathcal{U})}{\partial x_m} \right) - \left( \frac{\partial (b_m \mathcal{U})}{\partial x_m} \right)^2 \right\}. \quad (2)$$

Integrating over the domain,  $\Omega$ , using integration by parts, and the Leibniz rule gives

$$\begin{aligned} \frac{d}{dt} \int_{\Omega} \frac{\mathcal{U}^2}{2} d\Omega = \\ \frac{1}{2} \sum_{m=1}^3 \left( \oint_{\Gamma} \left\{ - (a_m \mathcal{U}^2) + 2\mathcal{U} \frac{(b_m \mathcal{U})}{\partial x_m} \right\} n_{x_m} d\Gamma - 2 \int_{\Omega} \left( \frac{\partial(b_m \mathcal{U})}{\partial x_m} \right)^2 d\Omega \right), \end{aligned} \quad (3)$$

where  $n_{x_m}$  is the  $m^{\text{th}}$  component of the outward facing unit normal. What Eq. (3) demonstrates is that the time rate of change of the norm of the solution,  $\|\mathcal{U}\|^2 \equiv \int_{\Omega} \mathcal{U}^2 d\Omega$ , depends on surface flux integrals and a viscous dissipation term. This implies that, in combination with appropriate boundary conditions, Eq. (3) results in a bound on the solution in terms of the data of the problem, and therefore a proof of stability. The SBP framework used in this paper is mimetic of the above energy stability analysis in a one-to-one fashion and results in similar stability statements for the semi-discrete equations.

Derivatives are approximated using differentiation matrices that are defined in computational space. To do so, Eq. (1) is transformed using the curvilinear coordinate transformation  $x_m = x_m(\xi_1, \xi_2, \xi_3)$ . Thus, on the  $\kappa^{\text{th}}$  element, the  $x_m$  derivatives are expanded using the chain rule as

$$\frac{\partial}{\partial x_m} = \sum_{l=1}^3 \frac{\partial \xi_l}{\partial x_m} \frac{\partial}{\partial \xi_l}, \quad \frac{\partial^2}{\partial x_m^2} = \sum_{l,a=1}^3 \frac{\partial \xi_l}{\partial x_m} \frac{\partial}{\partial \xi_l} \left( \frac{\partial \xi_a}{\partial x_m} \frac{\partial}{\partial \xi_a} \right).$$

Multiplying by the metric Jacobian,  $(\mathcal{J}_{\kappa})$ , Eq. (1) becomes

$$\mathcal{J}_{\kappa} \frac{\partial \mathcal{U}}{\partial t} + \sum_{l,m=1}^3 \mathcal{J}_{\kappa} \frac{\partial \xi_l}{\partial x_m} \frac{\partial (a_m \mathcal{U})}{\partial \xi_l} = \sum_{l,a,m=1}^3 \mathcal{J}_{\kappa} \frac{\partial \xi_l}{\partial x_m} \frac{\partial}{\partial \xi_l} \left( \frac{\partial \xi_a}{\partial x_m} \frac{\partial (b_m \mathcal{U})}{\partial \xi_a} \right). \quad (4)$$

Herein, Eq. (4) is referenced as the chain rule form of Eq. (1). Bringing the metric terms,  $\mathcal{J}_{\kappa} \frac{\partial \xi_l}{\partial x_m}$ , inside the derivative and using the product rule gives

$$\begin{aligned} \mathcal{J}_{\kappa} \frac{\partial \mathcal{U}}{\partial t} + \sum_{l,m=1}^3 \frac{\partial}{\partial \xi_l} \left( \mathcal{J}_{\kappa} \frac{\partial \xi_l}{\partial x_m} a_m \mathcal{U} \right) - \sum_{l,m=1}^3 a_m \mathcal{U} \frac{\partial}{\partial \xi_l} \left( \mathcal{J}_{\kappa} \frac{\partial \xi_l}{\partial x_m} \right) = \\ \sum_{l,a,m=1}^3 \frac{\partial}{\partial \xi_l} \left( \mathcal{J}_{\kappa} \frac{\partial \xi_l}{\partial x_m} \frac{\partial \xi_a}{\partial x_m} \frac{\partial (b_m \mathcal{U})}{\partial \xi_a} \right) - \sum_{l,a,m=1}^3 \frac{\partial \xi_a}{\partial x_m} \frac{\partial (b_m \mathcal{U})}{\partial \xi_a} \frac{\partial}{\partial \xi_l} \left( \mathcal{J}_{\kappa} \frac{\partial \xi_l}{\partial x_m} \right). \end{aligned} \quad (5)$$

The last terms on the left- and right-hand sides of (5) are zero via the GCL relations

$$\sum_{l=1}^3 \frac{\partial}{\partial \xi_l} \left( \mathcal{J}_{\kappa} \frac{\partial \xi_l}{\partial x_m} \right) = 0, \quad m = 1, 2, 3, \quad (6)$$

leading to the strong conservation form of the convection-diffusion equation in curvilinear coordinates:

$$\mathcal{J}_{\kappa} \frac{\partial \mathcal{U}}{\partial t} + \sum_{l,m=1}^3 \frac{\partial}{\partial \xi_l} \left( \mathcal{J}_{\kappa} \frac{\partial \xi_l}{\partial x_m} a_m \mathcal{U} \right) = \sum_{l,a,m=1}^3 \frac{\partial}{\partial \xi_l} \left( \mathcal{J}_{\kappa} \frac{\partial \xi_l}{\partial x_m} \frac{\partial \xi_a}{\partial x_m} \frac{\partial (b_m \mathcal{U})}{\partial \xi_a} \right). \quad (7)$$

The  $h$ -refinement procedure proceeds by subdividing the computational domain of parent elements; where children elements inherit the curvilinear coordinate transformation of the parent element. It is therefore convenient to introduce two computational coordinates:

- $\xi_l$ , which is the mapping from the child element to physical space, i.e., the computational coordinate system of the  $\kappa^{\text{th}}$  element,
- $\hat{\xi}_l$ , which is the mapping from the parent element to the physical space.

The mapping from children to parent elements is rectilinear. Thus, assuming that the child element has a computational domain of  $[-1, 1]^3$ , this transformation for the  $\kappa^{\text{th}}$  element is given by

$$\xi_l = \frac{2}{\Delta_l^\kappa} \hat{\xi}_l - \frac{(\hat{H}_\kappa^l + \hat{L}_\kappa^l)}{\Delta_l^\kappa}, \quad \Delta_l^\kappa \equiv \hat{H}_\kappa^l - \hat{L}_\kappa^l, \quad l = 1, 2, 3, \quad (8)$$

where  $\hat{H}_\kappa^l$  and  $\hat{L}_\kappa^l$  are the largest and smallest extent of the  $\xi_l$  coordinate in the coordinate system of the parent element ( $\hat{\xi}_l$ ). Using Eq. (8) the Jacobian and metrics are recast in terms of the Jacobian,  $\hat{\mathcal{J}}_\kappa$ , and metrics terms,  $\hat{\mathcal{J}}_\kappa \frac{\partial \hat{\xi}_l}{\partial x_m}$ , of the parent element. This step results in

$$\frac{\partial \xi_l}{\partial x_m} = \frac{2}{\Delta_l^\kappa} \frac{\partial \hat{\xi}_l}{\partial x_m}, \quad \mathcal{J}_\kappa = \frac{\Delta_1^\kappa \Delta_2^\kappa \Delta_3^\kappa}{8} \hat{\mathcal{J}}_\kappa, \quad \mathcal{J}_\kappa \frac{\partial \xi_l}{\partial x_m} = \frac{\Delta_1^\kappa \Delta_2^\kappa \Delta_3^\kappa}{4\Delta_l^\kappa} \hat{\mathcal{J}}_\kappa \frac{\partial \hat{\xi}_l}{\partial x_m}. \quad (9)$$

Inserting Eq. (9) into Eq. (4) and multiplying by  $8/(\Delta_1^\kappa \Delta_2^\kappa \Delta_3^\kappa)$  gives

$$\hat{\mathcal{J}}_\kappa \frac{\partial \mathcal{U}}{\partial t} + \sum_{l,m=1}^3 \frac{2}{\Delta_l^\kappa} \hat{\mathcal{J}}_\kappa \frac{\partial \hat{\xi}_l}{\partial x_m} \frac{\partial (a_m \mathcal{U})}{\partial \xi_l} = \sum_{l,a,m=1}^3 \frac{4}{\Delta_l^\kappa \Delta_a^\kappa} \hat{\mathcal{J}}_\kappa \frac{\partial \hat{\xi}_l}{\partial x_m} \left( \frac{\partial \hat{\xi}_a}{\partial x_m} \frac{\partial (b_m \mathcal{U})}{\partial \xi_a} \right). \quad (10)$$

Similarly, Eq. (5) is transformed to

$$\begin{aligned} & \hat{\mathcal{J}}_\kappa \frac{\partial \mathcal{U}}{\partial t} + \sum_{l,m=1}^3 \frac{2}{\Delta_l^\kappa} \frac{\partial}{\partial \xi_l} \left( \hat{\mathcal{J}}_\kappa \frac{\partial \hat{\xi}_l}{\partial x_m} a_m \mathcal{U} \right) - \sum_{l,m=1}^3 \frac{2}{\Delta_l^\kappa} a_m \mathcal{U} \frac{\partial}{\partial \xi_l} \left( \hat{\mathcal{J}}_\kappa \frac{\partial \hat{\xi}_l}{\partial x_m} \right) = \\ & \sum_{l,a,m=1}^3 \frac{4}{\Delta_l^\kappa \Delta_a^\kappa} \frac{\partial}{\partial \xi_l} \left( \hat{\mathcal{J}}_\kappa \frac{\partial \hat{\xi}_l}{\partial x_m} \frac{\partial \hat{\xi}_a}{\partial x_m} \frac{\partial (b_m \mathcal{U})}{\partial \xi_a} \right) \\ & - \sum_{l,a,m=1}^3 \frac{4}{\Delta_l^\kappa \Delta_a^\kappa} \frac{\partial \hat{\xi}_a}{\partial x_m} \frac{\partial (b_m \mathcal{U})}{\partial \xi_a} \frac{\partial}{\partial \xi_l} \left( \hat{\mathcal{J}}_\kappa \frac{\partial \hat{\xi}_l}{\partial x_m} \right), \end{aligned} \quad (11)$$

and Eq. (7) is transformed to

$$\begin{aligned} & \hat{\mathcal{J}}_\kappa \frac{\partial \mathcal{U}}{\partial t} + \sum_{l,m=1}^3 \frac{2}{\Delta_l^\kappa} \frac{\partial}{\partial \xi_l} \left( \hat{\mathcal{J}}_\kappa \frac{\partial \hat{\xi}_l}{\partial x_m} a_m \mathcal{U} \right) = \\ & \sum_{l,a,m=1}^3 \frac{4}{\Delta_l^\kappa \Delta_a^\kappa} \frac{\partial}{\partial \xi_l} \left( \hat{\mathcal{J}}_\kappa \frac{\partial \hat{\xi}_l}{\partial x_m} \frac{\partial \hat{\xi}_a}{\partial x_m} \frac{\partial (b_m \mathcal{U})}{\partial \xi_a} \right). \end{aligned} \quad (12)$$

Directly discretizing Eq. (12) leads to semi-discrete schemes that are not guaranteed to be stable. Instead, a well known approach is to use a canonical splitting of the inviscid terms which is constructed by using one half of the inviscid terms in (10) and one half of the inviscid terms in (11) (see, for instance, [9]). On the other hand, the viscous terms are treated in strong conservation form. This process results in

$$\begin{aligned} & \hat{\mathcal{J}}_\kappa \frac{\partial \mathcal{U}}{\partial t} + \frac{1}{2} \sum_{l,m=1}^3 \frac{2}{\Delta_l^\kappa} \left\{ \frac{\partial}{\partial \xi_l} \left( \hat{\mathcal{J}}_\kappa \frac{\partial \hat{\xi}_l}{\partial x_m} a_m \mathcal{U} \right) + \hat{\mathcal{J}}_\kappa \frac{\partial \hat{\xi}_l}{\partial x_m} \frac{\partial}{\partial \xi_l} (a_m \mathcal{U}) \right\} \\ & - \frac{1}{2} \sum_{l,m=1}^3 \left\{ a_m \mathcal{U} \frac{\partial}{\partial \xi_l} \left( \mathcal{J}_\kappa \frac{\partial \xi_l}{\partial x_m} \right) \right\} = \sum_{l,a,m=1}^3 \frac{4}{\Delta_l^\kappa \Delta_a^\kappa} \frac{\partial}{\partial \xi_l} \left( \hat{\mathcal{J}}_\kappa \frac{\partial \hat{\xi}_l}{\partial x_m} \frac{\partial \hat{\xi}_a}{\partial x_m} \frac{\partial (b_m \mathcal{U})}{\partial \xi_a} \right), \end{aligned} \quad (13)$$

where the last set of terms on the left-hand side are zero by the GCL conditions (6). Now, consider discretizing Eq. (13) by using the following differentiation matrices:

$$\mathbf{D}_{\xi_1} \equiv \mathbf{D}^{(1D)} \otimes \mathbf{I}_N \otimes \mathbf{I}_N, \quad \mathbf{D}_{\xi_2} \equiv \mathbf{I}_N \otimes \mathbf{D}^{(1D)} \otimes \mathbf{I}_N, \quad \mathbf{D}_{\xi_3} \equiv \mathbf{I}_N \otimes \mathbf{I}_N \otimes \mathbf{D}^{(1D)},$$

where  $\mathbf{I}_N$  is an  $N \times N$  identity matrix. The diagonal matrices containing the metric Jacobian and metric terms along their diagonals, respectively, are defined as follows:

$$\begin{aligned} \hat{\mathcal{J}}_\kappa & \equiv \text{diag} \left( \hat{\mathcal{J}}_\kappa \left( \boldsymbol{\xi}^{(1)} \right), \dots, \hat{\mathcal{J}}_\kappa \left( \boldsymbol{\xi}^{(N_\kappa)} \right) \right), \\ \left[ \hat{\mathcal{J}}_\kappa \frac{\partial \hat{\xi}_l}{\partial x_m} \right]_\kappa & \equiv \text{diag} \left( \hat{\mathcal{J}}_\kappa \frac{\partial \hat{\xi}_l}{\partial x_m} \left( \boldsymbol{\xi}^{(1)} \right), \dots, \hat{\mathcal{J}}_\kappa \frac{\partial \hat{\xi}_l}{\partial x_m} \left( \boldsymbol{\xi}^{(N_\kappa)} \right) \right), \end{aligned}$$

where  $N_\kappa \equiv N^3$  is the total number of nodes in the element  $\kappa$ . With these matrices, the discretization of (13) on the  $\kappa^{\text{th}}$  element is given as

$$\begin{aligned} & \hat{\mathcal{J}}_\kappa \frac{d\mathbf{u}_\kappa}{dt} + \frac{1}{2} \sum_{l,m=1}^3 \frac{2}{\Delta_l^\kappa} a_m \left\{ \mathbf{D}_{\xi_l} \left[ \hat{\mathcal{J}}_\kappa \frac{\partial \hat{\xi}_l}{\partial x_m} \right]_\kappa + \left[ \hat{\mathcal{J}}_\kappa \frac{\partial \hat{\xi}_l}{\partial x_m} \right]_\kappa \mathbf{D}_{\xi_l} \right\} \mathbf{u}_\kappa \\ & - \frac{1}{2} \sum_{l,m=1}^3 \left\{ \frac{2}{\Delta_l^\kappa} a_m \text{diag}(\mathbf{u}_\kappa) \mathbf{D}_{\xi_l} \left[ \hat{\mathcal{J}}_\kappa \frac{\partial \hat{\xi}_l}{\partial x_m} \right]_\kappa \mathbf{1}_\kappa \right\} = \\ & \sum_{l,m,a=1}^3 \frac{4}{\Delta_l^\kappa \Delta_a^\kappa} b_m \mathbf{D}_{\xi_l}^\kappa \hat{\mathcal{J}}_\kappa^{-1} \left[ \hat{\mathcal{J}}_\kappa \frac{\partial \hat{\xi}_l}{\partial x_m} \right]_\kappa \left[ \hat{\mathcal{J}}_\kappa \frac{\partial \hat{\xi}_a}{\partial x_m} \right]_\kappa \mathbf{D}_{\xi_a}^\kappa \mathbf{u}_\kappa, \end{aligned} \quad (14)$$

where  $\mathbf{1}_\kappa$  is a vector of ones of the size of the number of nodes on the  $\kappa^{\text{th}}$  element and the SATs have been dropped as they are not important for the current analysis. In the same way as in the continuous case, the semi-discrete equations have an associated set of discrete GCL conditions

$$\sum_{l=1}^3 \frac{2}{\Delta_l^\kappa} \mathbf{D}_{\xi_l} \left[ \hat{\mathcal{J}}_\kappa \frac{\partial \hat{\xi}_l}{\partial x_m} \right]_\kappa \mathbf{1}_\kappa = \mathbf{0}, \quad m = 1, 2, 3, \quad (15)$$



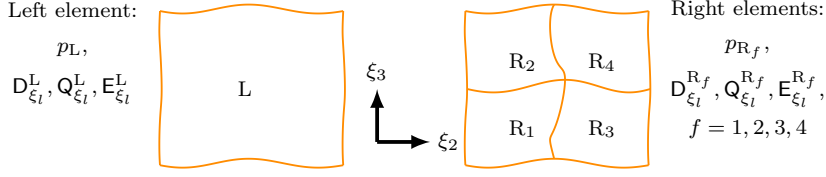


Fig. 1: Generic surface used to describe the construction of various quantities as well as to simplify the analysis of the semi-discrete schemes.

that if satisfied, lead to the following telescoping and therefore provably stable semi-discrete form:

$$\begin{aligned}
 \mathcal{J}_\kappa \frac{d\mathbf{u}_\kappa}{dt} + \frac{1}{2} \sum_{l,m=1}^3 \frac{2}{\Delta_l^\kappa} a_m \left\{ \mathcal{D}_{\xi_l} \left[ \hat{\mathcal{J}}_\kappa \frac{\partial \hat{\xi}_l}{\partial x_m} \right]_\kappa + \left[ \hat{\mathcal{J}}_\kappa \frac{\partial \hat{\xi}_l}{\partial x_m} \right]_\kappa \mathcal{D}_{\xi_l} \right\} \mathbf{u}_\kappa = \\
 \sum_{l,m,a=1}^3 \frac{4}{\Delta_l^\kappa \Delta_a^\kappa} b_m \mathcal{D}_{\xi_l}^\kappa \mathcal{J}_\kappa^{-1} \left[ \hat{\mathcal{J}}_\kappa \frac{\partial \hat{\xi}_l}{\partial x_m} \right]_\kappa \left[ \hat{\mathcal{J}}_\kappa \frac{\partial \hat{\xi}_a}{\partial x_m} \right]_\kappa \mathcal{D}_{\xi_a}^\kappa \mathbf{u}_\kappa.
 \end{aligned} \tag{16}$$

How to construct metrics that satisfy the discrete GCL conditions (15) will be detailed later in the paper and is one of the major contributions of this work. In the next subsection, attention is focused on the construction of appropriate interface coupling procedures that retain the stability (telescoping) properties of scheme (16) across  $h/p$  nonconforming elements (the pure  $p$  nonconforming case is detailed in [17, 18, 16]).

### 3.2 The nonconforming interface

To simplify both the analysis as well as the presentation of the semi-discrete scheme discussed in this paper, it is convenient to focus the attention only on a shared interface between two elements, one of which is  $h/p$ -refined. Without loss of generality, five elements are considered that have aligned computational coordinates and adjoin along a vertical interface; see Fig. 1. The focus is on nonconformities that arise from both  $h$  refinement/coarsening as well as local approximations with differing polynomial degrees, as would result from  $p$ -refinement/coarsening. Thus, the generic example, Fig. 1, that will be discussed considers a left element having polynomial degree  $p_L$  and a set of four right elements having polynomial degrees  $p_{R_f}$ ,  $f = 1, 2, 3, 4$ , possibly all having differing degree and not equal to  $p_L$  (i.e., they originate from a conforming right element that has been  $h$ -refined and then  $p$ -refined/coarsened). Therefore, the contributions from the left element are identified with subscript or superscript L and similarly for the right elements with subscripts or superscripts  $R_f$ ; see Fig. 1.

The analysis proceeds by developing macro matrix differentiation operators over the five elements, i.e., composed of elements L and  $R_f$ ,  $f = 1, 2, 3, 4$ , and then determining the required modifications/restrictions so that the resulting operators have the SBP property. A naive construction, in the computational coordinates of

the parent elements, would be the following operators:

$$\tilde{D}_{\hat{\xi}_l} \equiv \begin{bmatrix} D_{\hat{\xi}_l}^L & & & \\ & D_{\hat{\xi}_l}^{R_1} & & \\ & & \ddots & \\ & & & D_{\hat{\xi}_l}^{R_4} \end{bmatrix}, \quad l = 1, 2, 3, \quad (17)$$

where the element-wise components of the SBP operators, for example  $D_{\hat{\xi}_1}^L$ , are constructed as

$$D_{\hat{\xi}_1}^L \equiv \frac{2}{\Delta_1^L} D_{\xi_1}, \quad D_{\xi_1} \equiv D_L^{(1D)} \otimes I_L \otimes I_L,$$

$$P_L \equiv \frac{\Delta_1^L \Delta_2^L \Delta_3^L}{8} P_L^{(1D)} \otimes P_L^{(1D)} \otimes P_L^{(1D)},$$

$$Q_{\hat{\xi}_1}^L \equiv \frac{\Delta_2^L \Delta_3^L}{4} Q_L^{(1D)} \otimes P_L^{(1D)} \otimes P_L^{(1D)},$$

$$E_{\hat{\xi}_1}^L \equiv \frac{\Delta_2^L \Delta_3^L}{4} \left\{ e_N^L \left( e_N^L \right) \otimes P_L^{(1D)} \otimes P_L^{(1D)} - e_1^L \left( e_1^L \right) \otimes P_L^{(1D)} \otimes P_L^{(1D)} \right\},$$

where  $I_L$  is an identity matrix of size  $N_L^{1/3} \times N_L^{1/3}$  and  $N_L$  is the total number of nodes in element  $L$ .

While the  $\tilde{D}_{\hat{\xi}_2}$  and  $\tilde{D}_{\hat{\xi}_3}$  macro element operators are by construction SBP operators (i.e., they telescope to the boundaries), the  $\tilde{D}_{\hat{\xi}_1}$  is not an SBP operator. Moreover, the  $\tilde{D}_{\hat{\xi}_1}$  operator does not have any coupling between the elements. By using appropriate interface coupling, the  $\tilde{D}_{\hat{\xi}_1}$  operator can be modified so that the result is a macro element SBP operator. To accomplish this, interpolation operators are needed that interpolate information from elements  $R_f$  to element  $L$  and vice versa. For simplicity, the interpolation operators use only tensor product surface information from the adjoining interface surface.

With this background, general matrix difference operators between the five elements are constructed as

$$\tilde{D}_{\hat{\xi}_l} = \tilde{P}^{-1} \tilde{Q}_{\hat{\xi}_l} = \tilde{P}^{-1} \left( \tilde{S}_{\hat{\xi}_l} + \frac{1}{2} \tilde{E}_{\hat{\xi}_l} \right). \quad (18)$$

Focusing on the direction orthogonal to the interface ( $\xi_1$ ) the relevant matrices are given by

$$\begin{aligned}
\tilde{\mathbf{P}} &\equiv \text{diag}(\mathbf{P}_L, \mathbf{P}_{R_1}, \mathbf{P}_{R_2}, \mathbf{P}_{R_3}, \mathbf{P}_{R_4}), \\
\tilde{\mathbf{S}}_{\xi_1} &\equiv \begin{bmatrix} \mathbf{S}_{\xi_1}^L & \tilde{\mathbf{S}}_{12} & \tilde{\mathbf{S}}_{13} & \tilde{\mathbf{S}}_{14} & \tilde{\mathbf{S}}_{15} \\ \tilde{\mathbf{S}}_{21} & \mathbf{S}_{\xi_1}^{R_1} & & & \\ \tilde{\mathbf{S}}_{31} & & \mathbf{S}_{\xi_1}^{R_2} & & \\ \tilde{\mathbf{S}}_{41} & & & \mathbf{S}_{\xi_1}^{R_3} & \\ \tilde{\mathbf{S}}_{51} & & & & \mathbf{S}_{\xi_1}^{R_4} \end{bmatrix}, \\
\tilde{\mathbf{S}}_{12} &\equiv \frac{\Delta_2^L \Delta_3^L}{4} \mathbf{e}_N^L \left( \mathbf{e}_1^{R_1} \right)^T \mathbf{P}_L^{(1D)} \mathbf{l}_{R_1 \text{ to } L}^2 \otimes \mathbf{P}_L^{(1D)} \mathbf{l}_{R_1 \text{ to } L}^3, \\
\tilde{\mathbf{S}}_{21} &\equiv -\frac{\Delta_2^{R_1} \Delta_3^{R_1}}{4} \mathbf{e}_1^{R_1} \left( \mathbf{e}_N^L \right)^T \mathbf{P}_{R_1}^{(1D)} \mathbf{l}_{L \text{ to } R_1}^2 \otimes \mathbf{P}_{R_1}^{(1D)} \mathbf{l}_{L \text{ to } R_1}^3, \\
\tilde{\mathbf{S}}_{13} &\equiv \frac{\Delta_2^L \Delta_3^L}{4} \mathbf{e}_N^L \left( \mathbf{e}_1^{R_2} \right)^T \mathbf{P}_L^{(1D)} \mathbf{l}_{R_2 \text{ to } L}^2 \otimes \mathbf{P}_L^{(1D)} \mathbf{l}_{R_2 \text{ to } L}^3, \\
\tilde{\mathbf{S}}_{31} &\equiv -\frac{\Delta_2^{R_2} \Delta_3^{R_2}}{4} \mathbf{e}_1^{R_2} \left( \mathbf{e}_N^L \right)^T \mathbf{P}_{R_2}^{(1D)} \mathbf{l}_{L \text{ to } R_2}^2 \otimes \mathbf{P}_{R_2}^{(1D)} \mathbf{l}_{L \text{ to } R_2}^3, \\
\tilde{\mathbf{S}}_{14} &\equiv \frac{\Delta_2^L \Delta_3^L}{4} \mathbf{e}_N^L \left( \mathbf{e}_1^{R_3} \right)^T \mathbf{P}_L^{(1D)} \mathbf{l}_{R_3 \text{ to } L}^2 \otimes \mathbf{P}_L^{(1D)} \mathbf{l}_{R_3 \text{ to } L}^3, \\
\tilde{\mathbf{S}}_{41} &\equiv -\frac{\Delta_2^{R_3} \Delta_3^{R_3}}{4} \mathbf{e}_1^{R_3} \left( \mathbf{e}_N^L \right)^T \mathbf{P}_{R_3}^{(1D)} \mathbf{l}_{L \text{ to } R_3}^2 \otimes \mathbf{P}_{R_3}^{(1D)} \mathbf{l}_{L \text{ to } R_3}^3, \\
\tilde{\mathbf{S}}_{15} &\equiv \frac{\Delta_2^L \Delta_3^L}{4} \mathbf{e}_N^L \left( \mathbf{e}_1^{R_4} \right)^T \mathbf{P}_L^{(1D)} \mathbf{l}_{R_4 \text{ to } L}^2 \otimes \mathbf{P}_L^{(1D)} \mathbf{l}_{R_4 \text{ to } L}^3, \\
\tilde{\mathbf{S}}_{51} &\equiv -\frac{\Delta_2^{R_4} \Delta_3^{R_4}}{4} \mathbf{e}_1^{R_4} \left( \mathbf{e}_N^L \right)^T \mathbf{P}_{R_4}^{(1D)} \mathbf{l}_{L \text{ to } R_4}^2 \otimes \mathbf{P}_{R_4}^{(1D)} \mathbf{l}_{L \text{ to } R_4}^3, \\
\tilde{\mathbf{E}}_{\xi_1} &\equiv \begin{bmatrix} \tilde{\mathbf{E}}_{11} & & & & \\ & \tilde{\mathbf{E}}_{22} & & & \\ & & \ddots & & \\ & & & \tilde{\mathbf{E}}_{55} & \end{bmatrix}, \\
\tilde{\mathbf{E}}_{11} &\equiv -\frac{\Delta_2^L \Delta_3^L}{4} \mathbf{e}_1^L \left( \mathbf{e}_1^L \right)^T \otimes \mathbf{P}_L^{(1D)} \otimes \mathbf{P}_L^{(1D)}, \\
\tilde{\mathbf{E}}_{22} &\equiv \frac{\Delta_2^{R_1} \Delta_3^{R_1}}{4} \mathbf{e}_N^{R_1} \left( \mathbf{e}_N^{R_1} \right)^T \otimes \mathbf{P}_{R_1}^{(1D)} \otimes \mathbf{P}_{R_1}^{(1D)}, \\
\tilde{\mathbf{E}}_{55} &\equiv \frac{\Delta_2^{R_4} \Delta_3^{R_4}}{4} \mathbf{e}_N^{R_4} \left( \mathbf{e}_N^{R_4} \right)^T \otimes \mathbf{P}_{R_4}^{(1D)} \otimes \mathbf{P}_{R_4}^{(1D)},
\end{aligned} \tag{19}$$

and  $\mathbf{l}_{R_f \text{ to } L}^l$  and  $\mathbf{l}_{L \text{ to } R_f}^l$  are one-dimensional interpolation operators, in the  $l$  direction, from the  $R_f$  element to the  $L$  element and vice versa.

A necessary constraint that the SBP formalism places on  $\tilde{\mathbf{D}}_{\xi_1}$  is skew-symmetry of the  $\tilde{\mathbf{S}}_{\xi_1}$  matrices. The block-diagonal matrices in  $\tilde{\mathbf{S}}_{\xi_1}$  are already skew-symmetric but the off diagonal blocks are not. Thus, it is necessary to satisfy the following conditions:

$$\tilde{\mathbf{S}}_{12} = -\tilde{\mathbf{S}}_{21}^T, \quad \tilde{\mathbf{S}}_{13} = -\tilde{\mathbf{S}}_{31}^T, \quad \tilde{\mathbf{S}}_{14} = -\tilde{\mathbf{S}}_{41}^T.$$

This implies that the interpolation operators are related to each other as follows:

$$\mathbf{l}_{R_f \text{ to } L}^l = \frac{\Delta_L^{R_f}}{\Delta_L^f} \left( \mathbf{P}_L^{(1D)} \right)^{-1} \left( \mathbf{l}_{L \text{ to } R_f}^l \right)^T \mathbf{P}_{R_1}^{(1D)}, \quad l = 1, 2, \quad f = 1, 2, 3, 4.$$

This property is denoted as the SBP preserving property because it leads to a macro element differentiation matrix that is an SBP operator. The interpolation operators from the left element to the right elements is constructed using an  $L_2$  projection approach such that

$$\begin{aligned} \mathbf{l}_{L \text{ to } R_f}^l &\equiv \left( \mathbf{M}_{R_f}^{\hat{\xi}_l} \right)^{-1} \mathbf{M}_{L \text{ to } R_f}^{\hat{\xi}_l}, \\ \mathbf{M}_{R_f}^{\hat{\xi}_l}(i, j) &\equiv \int_{\hat{L}_{R_f}^l}^{\hat{H}_{R_f}^l} \mathcal{L}_{\hat{\xi}_l, R_f}^{(i)} \mathcal{L}_{\hat{\xi}_l, R_f}^{(j)} d\hat{\xi}_l, \quad i, j = 1, \dots, (p_{R_f} + 1), \\ \mathbf{M}_{L \text{ to } R_f}^{\hat{\xi}_l}(i, j) &\equiv \int_{\hat{L}_{R_f}^l}^{\hat{H}_{R_f}^l} \mathcal{L}_{\hat{\xi}_l, R_f}^{(i)} \mathcal{L}_{\hat{\xi}_l, L}^{(j)} d\hat{\xi}_l, \quad i = 1, \dots, (p_{R_f} + 1) \quad j = 1, \dots, (p_L + 1), \end{aligned}$$

where  $\mathcal{L}_{\hat{\xi}_l, R_f}^{(i)}$  and  $\mathcal{L}_{\hat{\xi}_l, L}^{(j)}$  are the  $i^{\text{th}}$  and  $j^{\text{th}}$  Lagrange basis functions constructed from the nodes of element  $R_f$  and  $L$  in the parent elements coordinates, respectively. Now theorems on the accuracy of the interpolation operators are presented

**Theorem 1** *The interpolation operator  $\mathbf{l}_{L \text{ to } R_f}^l$  is of degree  $\min(N_L^{1/3} - 1, N_{R_f}^{1/3} - 1)$ .*

*Proof* The proof is standard and is not included for brevity. It follows by expanding out the matrices and taking advantage of the interpolating property of the Lagrangian basis functions.

The interpolation operators  $\mathbf{l}_{R_f \text{ to } L}^l$  individually are not polynomial exact, but rather, their combination is.

**Theorem 2** *The combined interpolation from the right elements to the left element is of degree  $\min(N_L - 2, N_{R_1} - 2, \dots, N_{R_4} - 2)$ , if the norms are suboptimal, i.e., degree  $2p - 1$ , otherwise it is of degree  $\min(N_L - 1, N_{R_1} - 1, \dots, N_{R_4} - 1)$ . In the five-element example used herein, the combined interpolation operator, acting on some function  $\mathcal{U}$ , is*

$$\mathbf{l}_{R_1 \text{ to } L} \mathbf{u}_{R_1} + \mathbf{l}_{R_2 \text{ to } L} \mathbf{u}_{R_2} + \mathbf{l}_{R_3 \text{ to } L} \mathbf{u}_{R_3} + \mathbf{l}_{R_4 \text{ to } L} \mathbf{u}_{R_4},$$

where  $\mathbf{u}_{R_f}$  is the vector containing the evaluation of the function  $\mathcal{U}$  at the nodes of the abutting surface of the  $R_f$  element and

$$\mathbf{l}_{R_f \text{ to } L} \equiv \mathbf{l}_{R_f \text{ to } L}^2 \otimes \mathbf{l}_{R_f \text{ to } L}^3, \quad f = 1, 2, 3, 4.$$

*Proof* This proof follows in the same way as proven elsewhere, for example, see [27].

The semi-discrete skew-symmetric split operator given in Eq. (13), discretized using the macro element operators  $\tilde{\mathbf{D}}_{\hat{\xi}_l}$ , and metric terms,  $\hat{\mathbf{J}}, \left[ \mathcal{J} \frac{\partial \xi_l}{\partial x_m} \right]$ , leads to the

following scheme:

$$\begin{aligned} \mathring{J} \frac{d\tilde{\mathbf{u}}}{dt} + \frac{1}{2} \sum_{l,m=1}^3 a_m \left( \tilde{\mathbf{D}}_{\hat{\xi}_l} \left[ \hat{\mathcal{J}}_{\kappa} \frac{\partial \hat{\xi}_l}{\partial x_m} \right] + \left[ \hat{\mathcal{J}}_{\kappa} \frac{\partial \hat{\xi}_l}{\partial x_m} \right] \tilde{\mathbf{D}}_{\hat{\xi}_l} \right) \tilde{\mathbf{u}} \\ - \frac{1}{2} \sum_{l,m=1}^3 a_m \text{diag}(\tilde{\mathbf{u}}) \tilde{\mathbf{D}}_{\hat{\xi}_l} \left[ \hat{\mathcal{J}}_{\kappa} \frac{\partial \hat{\xi}_l}{\partial x_m} \right] \tilde{\mathbf{1}} = \sum_{l,a=1}^3 \tilde{\mathbf{D}}_{\hat{\xi}_l} [\hat{\mathcal{C}}_{l,a}] \tilde{\mathbf{D}}_{\hat{\xi}_a}, \end{aligned} \quad (20)$$

where

$$\begin{aligned} \tilde{\mathbf{u}} &\equiv \left[ \mathbf{u}_{\text{L}}^{\text{T}}, \mathbf{u}_{\text{R}_1}^{\text{T}}, \mathbf{u}_{\text{R}_2}^{\text{T}}, \mathbf{u}_{\text{R}_3}^{\text{T}}, \mathbf{u}_{\text{R}_4}^{\text{T}} \right]^{\text{T}}, \mathring{J} \equiv \text{diag} \begin{bmatrix} \mathring{J}_{\text{L}} & & & & \\ & \mathring{J}_{\text{R}_1} & & & \\ & & \ddots & & \\ & & & \ddots & \\ & & & & \mathring{J}_{\text{R}_4} \end{bmatrix}, \\ \left[ \hat{\mathcal{J}}_{\kappa} \frac{\partial \hat{\xi}_l}{\partial x_m} \right] &\equiv \begin{bmatrix} \left[ \hat{\mathcal{J}}_{\kappa} \frac{\partial \hat{\xi}_l}{\partial x_m} \right]_{\text{L}} & & & & \\ & \left[ \hat{\mathcal{J}}_{\kappa} \frac{\partial \hat{\xi}_l}{\partial x_m} \right]_{\text{R}_1} & & & \\ & & \ddots & & \\ & & & \ddots & \\ & & & & \left[ \hat{\mathcal{J}}_{\kappa} \frac{\partial \hat{\xi}_l}{\partial x_m} \right]_{\text{R}_4} \end{bmatrix}, \\ \left[ \hat{\mathcal{C}}_{l,a} \right] &\equiv \sum_{m=1}^3 b_m \left[ \hat{\mathcal{J}}_{\kappa} \frac{\partial \hat{\xi}_l}{\partial x_m} \right] = \begin{bmatrix} \left[ \hat{\mathcal{C}}_{l,a} \right]_{\text{L}} & & & & \\ & \left[ \hat{\mathcal{C}}_{l,m} \right]_{\text{R}_1} & & & \\ & & \ddots & & \\ & & & \ddots & \\ & & & & \left[ \hat{\mathcal{C}}_{l,m} \right]_{\text{R}_4} \end{bmatrix}. \end{aligned} \quad (21)$$

As was the case in Eq. (14), a necessary condition for stability is that the metric terms satisfy the following discrete GCL conditions:

$$\sum_{l=1}^3 \tilde{\mathbf{D}}_{\hat{\xi}_l} \left[ \hat{\mathcal{J}}_{\kappa} \frac{\partial \hat{\xi}_l}{\partial x_m} \right] \tilde{\mathbf{1}} = \mathbf{0}. \quad (22)$$

Unfortunately, since  $\tilde{\mathbf{D}}_{\hat{\xi}_l}$  is not a tensor product operator and therefore in general does not commute with the other derivative matrix operators, discrete metrics constructed using the analytic formalism of Vinokur and Yee [50] or Thomas and Lombard [49] will not in general satisfy the discrete GCL condition required in Eq. (22). This means that instead, the metric terms have to be constructed so that they directly satisfy the GCL constraints.

*Remark 1* The metric terms are assigned colors; e.g., the time-term Jacobian:  $\mathring{J}$  or the volume metric terms:  $\left[ \hat{\mathcal{J}}_{\kappa} \frac{\partial \hat{\xi}_l}{\partial x_m} \right]$ . Metric terms with common colors form a set that must be computed consistently. For example, the time-term Jacobian and the volume metric Jacobian may not be computed in the same way. Another important set are the surface metrics are introduced in the next subsection.

### 3.3 Isolating the metric terms

The discrete GCL system (22) is highly under-determined and couples the approximation of the metric terms in all five elements. In general, the resulting GCL conditions for arbitrary  $h/p$ -refinement would couple large sets of elements making the solution of (22) difficult if not impossible. Note that the GCL conditions originate from the spatial discretization of the skew-symmetric splitting of the convective terms. Thus, if the approximation for those terms can be appropriately modified then a set of element-local discrete GCL conditions can be constructed making the problem tractable again. This is precisely the approach taken in [18, 17, 16] in the context of  $p$ -refinement/coarsening, and it is the same procedure used herein.

Examining the volume terms for the approximation of the skew-symmetric splitting highlights how to decouple the discrete GCL conditions:

$$\begin{aligned}
& \tilde{\mathbf{P}} \left( \tilde{\mathbf{D}}_{\hat{\xi}_1} \left[ \hat{\mathcal{J}}_{\kappa} \frac{\partial \hat{\xi}_1}{\partial x_m} \right] + \left[ \hat{\mathcal{J}}_{\kappa} \frac{\partial \hat{\xi}_1}{\partial x_m} \right] \tilde{\mathbf{D}}_{\hat{\xi}_1} \right) = \\
& \begin{bmatrix} \mathbf{A}_{11} & \mathbf{A}_{12} & \mathbf{A}_{13} & \mathbf{A}_{14} & \mathbf{A}_{15} \\ -\mathbf{A}_{12}^T & \mathbf{A}_{22} & & & \\ -\mathbf{A}_{13}^T & & \mathbf{A}_{33} & & \\ -\mathbf{A}_{14}^T & & & \mathbf{A}_{44} & \\ -\mathbf{A}_{15}^T & & & & \mathbf{A}_{55} \end{bmatrix} + \left( \tilde{\mathbf{E}}_{\hat{\xi}_1} \left[ \hat{\mathcal{J}}_{\kappa} \frac{\partial \hat{\xi}_1}{\partial x_m} \right] + \left[ \hat{\mathcal{J}}_{\kappa} \frac{\partial \hat{\xi}_1}{\partial x_m} \right] \tilde{\mathbf{E}}_{\hat{\xi}_1} \right), \\
& \mathbf{A}_{11} \equiv \left\{ \mathbf{S}_{\hat{\xi}_1}^L \left[ \hat{\mathcal{J}}_{\kappa} \frac{\partial \hat{\xi}_1}{\partial x_m} \right]_L + \left[ \hat{\mathcal{J}}_{\kappa} \frac{\partial \hat{\xi}_1}{\partial x_m} \right]_L \mathbf{S}_{\hat{\xi}_1}^L \right\}, \\
& \mathbf{A}_{1f} = \frac{\Delta_2^L \Delta_3^L}{4} \left\{ \left[ \hat{\mathcal{J}}_{\kappa} \frac{\partial \hat{\xi}_1}{\partial x_m} \right]_L \left( \mathbf{e}_N^L \left( \mathbf{e}_1^{R_f} \right)^T \otimes \mathbf{P}_L^{(1D)} \mathbf{I}_{R_f \text{ to } L}^2 \otimes \mathbf{P}_L^{(1D)} \mathbf{I}_{R_f \text{ to } L}^3 \right) \right. \\
& \quad \left. + \left( \mathbf{e}_N^L \left( \mathbf{e}_1^{R_f} \right)^T \otimes \mathbf{P}_L^{(1D)} \mathbf{I}_{R_f \text{ to } L}^2 \otimes \mathbf{P}_L^{(1D)} \mathbf{I}_{R_f \text{ to } L}^3 \right) \left[ \hat{\mathcal{J}}_{\kappa} \frac{\partial \hat{\xi}_1}{\partial x_m} \right]_{R_f} \right\}, \\
& \mathbf{A}_{ff} \equiv \left\{ \mathbf{S}_{\hat{\xi}_1}^{R_f} \left[ \hat{\mathcal{J}}_{\kappa} \frac{\partial \hat{\xi}_1}{\partial x_m} \right]_{R_f} + \left[ \hat{\mathcal{J}}_{\kappa} \frac{\partial \hat{\xi}_1}{\partial x_m} \right]_{R_f} \mathbf{S}_{\hat{\xi}_1}^{R_f} \right\}, \quad f = 1, 2, 3, 4.
\end{aligned} \tag{23}$$

The highlighted terms are responsible for the weak coupling in the discrete GCL constraints. Note that these can be replaced with any design order quantities. The approach taken here to decouple the discrete GCL conditions is to zero the terms associated with the surface metrics on the element L, i.e., the terms  $\left[ \hat{\mathcal{J}}_{\kappa} \frac{\partial \hat{\xi}_1}{\partial x_m} \right]_L$  and to specify the terms on the  $R_f$  elements, i.e.,  $\left[ \hat{\mathcal{J}}_{\kappa} \frac{\partial \hat{\xi}_1}{\partial x_m} \right]_{R_f}$ .

*Remark 2* In contrast to the  $p$ -adaptation case [17, 18, 16], we do not use surface metric terms from both sides of the element. This is because using surface metric terms from the L element results in a coupled system of equations for the GCL conditions (22).

The action of the interface coupling is illustrated in Fig. 2. Using the above

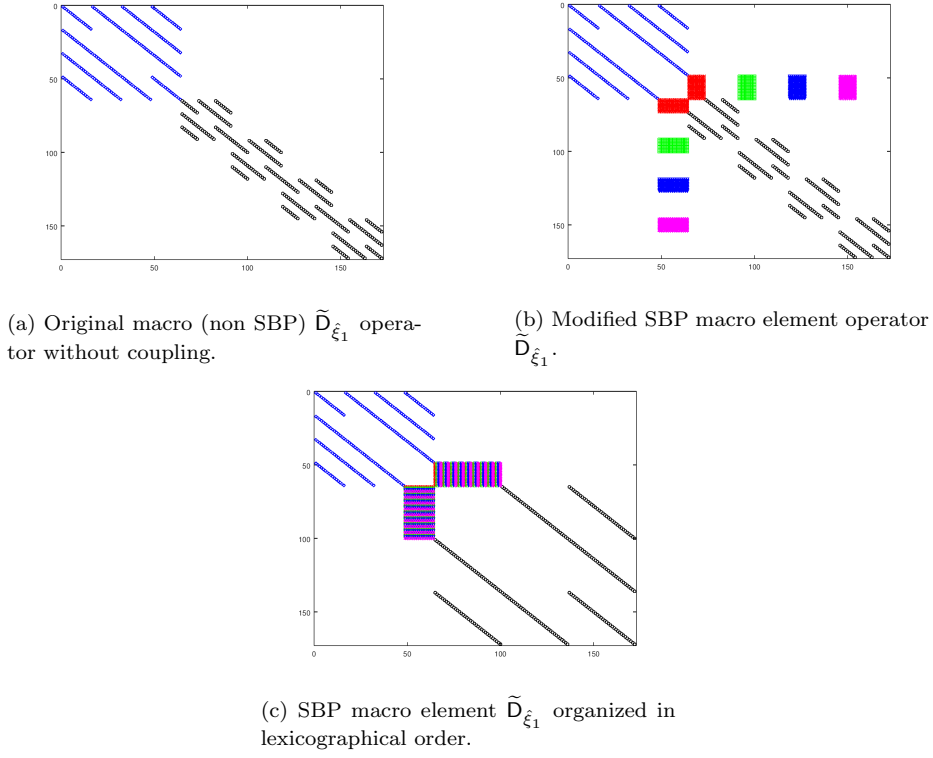


Fig. 2: Non-zero pattern of the various macro  $\tilde{D}_{\xi_1}$  operators.

approach, the discrete GCL conditions (22) become (where contributions from the boundary SATs have been ignored)

$$\begin{aligned}
& \sum_{l=1}^3 \mathbf{D}_{\xi_l}^L \left[ \hat{\mathcal{J}}_{\kappa} \frac{\partial \hat{\xi}_l}{\partial x_m} \right]_{\mathbf{L}} \mathbf{1}_{\mathbf{L}} = \\
& \frac{\Delta_2^{\mathbf{R}_f} \Delta_3^{\mathbf{R}_f}}{4} (\mathbf{P}^L)^{-1} \left\{ \mathbf{R}_L^T (\mathbf{P}_L^{(1D)} \otimes \mathbf{P}_L^{(1D)}) \mathbf{R}_L \left[ \hat{\mathcal{J}}_{\kappa} \frac{\partial \hat{\xi}_1}{\partial x_m} \right]_{\mathbf{L}} \right\} \mathbf{1}_{\mathbf{L}} \\
& - \frac{\Delta_2^{\mathbf{R}_f} \Delta_3^{\mathbf{R}_f}}{4} (\mathbf{P}^L)^{-1} \sum_{f=1}^4 \left\{ \mathbf{R}_L^T (\mathbf{P}_L^{(1D)})_{\mathbf{R}_f \text{ to } \mathbf{L}}^2 \otimes \mathbf{P}_L^{(1D)}_{\mathbf{R}_f \text{ to } \mathbf{L}}^3 \left[ \hat{\mathcal{J}}_{\kappa} \frac{\partial \hat{\xi}_1}{\partial x_m} \right]_{\mathbf{R}_f}^{\hat{T}} \mathbf{R}_{\mathbf{R}_f} \right\} \mathbf{1}_{\mathbf{R}_f},
\end{aligned} \tag{24}$$

$$\begin{aligned}
& \sum_{l=1}^3 D_{\hat{\xi}_l}^{\text{R}_f} \left[ \hat{\mathcal{J}}_{\kappa} \frac{\partial \hat{\xi}_l}{\partial x_m} \right]_{\text{R}_f} \mathbf{1}_{\text{R}_f} = \\
& - \frac{\Delta_2^{\text{R}_f} \Delta_3^{\text{R}_f}}{4} \left( \mathbf{P}^{\text{R}_f} \right)^{-1} \left\{ \mathbf{R}_{\text{R}_f}^{\text{T}} \left( \mathbf{P}_{\text{R}_f}^{(1D)} \otimes \mathbf{P}_{\text{R}_f}^{(1D)} \right) \mathbf{R}_{\text{R}_f} \left[ \hat{\mathcal{J}}_{\kappa} \frac{\partial \hat{\xi}_1}{\partial x_m} \right]_{\text{R}_f} \right\} \mathbf{1}_{\text{R}_f} \\
& + \frac{\Delta_2^{\text{R}_f} \Delta_3^{\text{R}_f}}{4} \left( \mathbf{P}^{\text{R}_f} \right)^{-1} \left\{ \mathbf{R}_{\text{R}_f}^{\text{T}} \left[ \hat{\mathcal{J}}_{\kappa} \frac{\partial \hat{\xi}_1}{\partial x_m} \right]_{\text{R}_f}^{\hat{\Gamma}} \left( \mathbf{P}_{\text{R}_f}^{(1D)} \mathbf{l}_{\text{LtoR}_f}^2 \otimes \mathbf{P}_{\text{R}_f}^{(1D)} \mathbf{l}_{\text{LtoR}_f}^3 \right) \mathbf{R}_{\text{L}} \right\} \mathbf{1}_{\text{L}},
\end{aligned} \tag{25}$$

where

$$\mathbf{R}_{\text{L}} \equiv \left( \mathbf{e}_N^{\text{L}} \right)^{\text{T}} \otimes \mathbf{l}_{\text{L}} \otimes \mathbf{l}_{\text{L}}, \quad \mathbf{R}_{\text{R}_f} \equiv \left( \mathbf{e}_1^{\text{R}_f} \right)^{\text{T}} \otimes \mathbf{l}_{\text{R}_f} \otimes \mathbf{l}_{\text{R}_f}.$$

The matrices  $\left[ \hat{\mathcal{J}}_{\kappa} \frac{\partial \hat{\xi}_1}{\partial x_m} \right]_{\text{R}_f}^{\hat{\Gamma}}$  are of size  $N_{\text{R}_f}^{2/3} \times N_{\text{R}_f}^{2/3}$  and their diagonal elements are approximations to the metrics on the surface nodes of element  $\text{R}_f$  at the shared interface. In order to decouple the five systems of equations in (24) and (25) the terms in  $\left[ \hat{\mathcal{J}}_{\kappa} \frac{\partial \hat{\xi}_1}{\partial x_m} \right]_{\text{R}_f}^{\hat{\Gamma}}$  need to be specified, for example, using the analytic metrics, which is the approach taken in this paper. For later use, we introduce notation for the macro element  $\tilde{\mathbf{D}}_{l,m}$  which is the macro element operator constructed as described above for the metric terms  $\hat{\mathcal{J}}_{\kappa} \frac{\partial \hat{\xi}_l}{\partial x_m}$ .

The next section reviews how to construct the metrics so that the discrete GCL conditions (24) and (25) are satisfied.

### 3.4 Metric solution mechanics

This section details the approximation of the metric terms so that entropy stability and free-stream preservation are maintained. There are two sets of metrics that need to be approximated, the volume metrics and the surface metrics. What needs to be satisfied are the discrete GCL equations (24) and (25), which are recast below in a form that is more convenient for developing a solution procedure. Thus, multiplying the discrete GCL constraints by  $-1$ , using the SBP property  $\mathbf{Q} = -\mathbf{Q}^{\text{T}} + \mathbf{E}$ , and simplifying the expressions gives

$$\begin{aligned}
& \sum_{l=1}^3 \left( \mathbf{Q}_{\hat{\xi}_l}^{\text{L}} \right)^{\text{T}} \left[ \hat{\mathcal{J}}_{\kappa} \frac{\partial \hat{\xi}_l}{\partial x_m} \right]_{\text{L}} \mathbf{1}_{\text{L}} = \\
& \frac{\Delta_2^{\text{R}_f} \Delta_3^{\text{R}_f}}{4} \sum_{f=1}^4 \left\{ \mathbf{R}_{\text{L}}^{\text{T}} \left( \mathbf{P}_{\text{L}}^{(1D)} \mathbf{l}_{\text{R}_f\text{toL}}^2 \otimes \mathbf{P}_{\text{L}}^{(1D)} \mathbf{l}_{\text{R}_f\text{toL}}^3 \right) \left[ \hat{\mathcal{J}}_{\kappa} \frac{\partial \hat{\xi}_1}{\partial x_m} \right]_{\text{R}_f}^{\hat{\Gamma}} \mathbf{R}_{\text{R}_f} \right\} \mathbf{1}_{\text{R}_f},
\end{aligned} \tag{26}$$



$$\sum_{l=1}^3 \mathbf{Q}_{\hat{\xi}_l}^{\mathbf{R}_f} \left[ \hat{\mathcal{J}}_{\kappa} \frac{\partial \hat{\xi}_l}{\partial x_m} \right]_{\mathbf{R}_f} \mathbf{1}_{\mathbf{R}_f} = - \frac{\Delta_2^{\mathbf{R}_f} \Delta_3^{\mathbf{R}_f}}{4} \left( \mathbf{P}^{\mathbf{R}_f} \right)^{-1} \left\{ \mathbf{R}_{\mathbf{R}_f}^{\mathbf{T}} \left[ \hat{\mathcal{J}}_{\kappa} \frac{\partial \hat{\xi}_1}{\partial x_m} \right]_{\mathbf{R}_f}^{\hat{\Gamma}} \left( \mathbf{P}_{\mathbf{R}_f}^{(1D)} \mathbf{l}_{\mathbf{L} \text{ to } \mathbf{R}_f}^2 \otimes \mathbf{P}_{\mathbf{R}_f}^{(1D)} \mathbf{l}_{\mathbf{L} \text{ to } \mathbf{R}_f}^3 \right) \mathbf{R}_{\mathbf{L}} \right\} \mathbf{1}_{\mathbf{L}}, \quad (27)$$

where  $\mathbf{l}_{\mathbf{R}_f}$  is an identity matrix of size  $N_{\mathbf{R}_f}^{1/3} \times N_{\mathbf{R}_f}$  and  $N_{\mathbf{R}_f}$  is the total number of nodes in element  $\mathbf{R}_f$ .

Note that the contributions from the  $\mathbf{E}_{\hat{\xi}_l}$  from the left-hand side (i.e., coming from the step  $\mathbf{Q} = -\mathbf{Q}^{\mathbf{T}} + \mathbf{E}$ ) related to the boundaries of the macro element are ignored. This contributions interact with the boundary SATs in the same way as the interface does.

The metric terms in Eq. (26) and Eq. (27) are set by solving a strictly convex quadratic optimization problem, based on the algorithm proposed in Crean *et al.* [12] (see also [18, 16]). Here the procedure is exemplified in terms of the discrete GCL system on the L element:

$$\begin{aligned} \min_{\mathbf{a}_m^{\mathbf{L}}} & \frac{1}{2} \left( \mathbf{a}_m^{\mathbf{L}} - \mathbf{a}_{m, \text{target}}^{\mathbf{L}} \right)^{\mathbf{T}} \left( \mathbf{a}_m^{\mathbf{L}} - \mathbf{a}_{m, \text{target}}^{\mathbf{L}} \right), \\ \text{subject to } & \mathbf{M}^{\mathbf{L}} \mathbf{a}_m^{\mathbf{L}} = \mathbf{c}_m^{\mathbf{L}}, \quad m = 1, 2, 3, \end{aligned} \quad (28)$$

where the vectors  $\mathbf{a}_m^{\mathbf{L}}$  and  $\mathbf{a}_{m, \text{target}}^{\mathbf{L}}$  are the optimized and target volume metric terms, respectively. Herein, the analytic metric terms are the target volume metrics. Furthermore,

$$\begin{aligned} \left( \mathbf{a}_m^{\mathbf{L}} \right)^{\mathbf{T}} & \equiv \mathbf{1}_{\mathbf{L}}^{\mathbf{T}} \left[ \left[ \hat{\mathcal{J}}_{\kappa} \frac{\partial \hat{\xi}_1}{\partial x_m} \right]_{\mathbf{L}}, \left[ \hat{\mathcal{J}}_{\kappa} \frac{\partial \hat{\xi}_2}{\partial x_m} \right]_{\mathbf{L}}, \left[ \hat{\mathcal{J}}_{\kappa} \frac{\partial \hat{\xi}_3}{\partial x_m} \right]_{\mathbf{L}} \right], \\ \mathbf{M}^{\mathbf{L}} & \equiv \left[ \left( \mathbf{Q}_{\hat{\xi}_1}^{\mathbf{L}} \right)^{\mathbf{T}}, \left( \mathbf{Q}_{\hat{\xi}_2}^{\mathbf{L}} \right)^{\mathbf{T}}, \left( \mathbf{Q}_{\hat{\xi}_3}^{\mathbf{L}} \right)^{\mathbf{T}} \right], \end{aligned}$$

and

$$\mathbf{c}_m^{\mathbf{L}} \equiv \frac{\Delta_2^{\mathbf{R}_f} \Delta_3^{\mathbf{R}_f}}{4} \sum_{f=1}^4 \left\{ \mathbf{R}_{\mathbf{L}}^{\mathbf{T}} \left( \mathbf{P}_{\mathbf{L}}^{(1D)} \mathbf{l}_{\mathbf{R}_f \text{ to } \mathbf{L}}^2 \otimes \mathbf{P}_{\mathbf{L}}^{(1D)} \mathbf{l}_{\mathbf{R}_f \text{ to } \mathbf{L}}^3 \right) \left[ \hat{\mathcal{J}}_{\kappa} \frac{\partial \hat{\xi}_1}{\partial x_m} \right]_{\mathbf{R}_f}^{\hat{\Gamma}} \mathbf{R}_{\mathbf{R}_f} \right\} \mathbf{1}_{\mathbf{R}_f},$$

with  $\mathbf{a}_m^{\mathbf{L}}$  of size  $3N_{\mathbf{L}} \times 1$ ,  $\mathbf{M}^{\mathbf{L}}$  of size  $N_{\mathbf{L}} \times 3N_{\mathbf{L}}$ , and  $\mathbf{c}_m^{\mathbf{L}}$  of size  $N_{\mathbf{L}} \times 1$ , where  $N_{\mathbf{L}}$  is the total number of nodes in element L. The optimal solution, in the Cartesian 2-norm, is given by (see Proposition 1 in Crean *et al.* [12])

$$\mathbf{a}_m^{\mathbf{L}} = \mathbf{a}_{m, \text{target}}^{\mathbf{L}} - \left( \mathbf{M}^{\mathbf{L}} \right)^{\dagger} \left( \mathbf{M}^{\mathbf{L}} \mathbf{a}_{m, \text{target}}^{\mathbf{L}} - \mathbf{c}_m^{\mathbf{L}} \right), \quad (29)$$

where  $\left( \mathbf{M}^{\mathbf{L}} \right)^{\dagger}$  is the Moore–Penrose pseudo inverse of  $\mathbf{M}^{\mathbf{L}}$ . This pseudo inverse is computed using a singular value decomposition of  $\mathbf{M}^{\mathbf{L}}$

$$\mathbf{M}^{\mathbf{L}} = \mathbf{U}^{\mathbf{L}} \mathbf{\Sigma}^{\mathbf{L}} \left( \mathbf{V}^{\mathbf{L}} \right)^{\mathbf{T}}, \quad \left( \mathbf{M}^{\mathbf{L}} \right)^{\dagger} = \mathbf{V}^{\mathbf{L}} \left( \mathbf{\Sigma}^{\mathbf{L}} \right)^{\dagger} \left( \mathbf{U}^{\mathbf{L}} \right)^{\mathbf{T}}.$$

The unitary matrix  $\mathbf{U}^L$  is of size  $N_L \times N_L$ ,  $\boldsymbol{\Sigma}^L$  is a diagonal matrix of size  $N_L \times N_L$  containing the singular values of  $\mathbf{M}^L$ , and  $(\mathbf{V}^L)^T$  is of size  $N_L \times 3N_L$  with orthonormal rows. The optimal solution  $\mathbf{a}_m^L$  given by (29) satisfies the discrete GCL relations (26) if the following constraint is satisfied:

$$\mathbf{1}_L^T \mathbf{c}_m^L = 0. \quad (30)$$

The constraint (30) is a discrete approximation to the integral of the GCL equations over the domain  $\hat{\Omega}_L$ , i.e.

$$\mathbf{1}_L^T \mathbf{c}_m^L \approx \int_{\hat{\Omega}_L} \sum_{l=1}^3 \frac{\partial}{\partial \hat{\xi}_l} \left( \hat{\mathcal{J}}_\kappa \frac{\partial \hat{\xi}_l}{\partial x_m} \right) d\hat{\Omega} = \oint_{\hat{\Gamma}_L} \sum_{l=1}^3 \hat{\mathcal{J}}_\kappa \frac{\partial \hat{\xi}_l}{\partial x_m} n_{\hat{\xi}_l} d\hat{\Gamma} = 0. \quad (31)$$

In fact, our approach is to specify the surface metric terms  $\left[ \hat{\mathcal{J}}_\kappa \frac{\partial \hat{\xi}_l}{\partial x_m} \right]_{R_f}^{\hat{\Gamma}}$  such that  $\mathbf{1}_L^T \mathbf{c}_m^L$  is exactly equal to the surface integral term on the RHS of (31).

The constraint (30) arises because  $\mathbf{M}^L$  has one zero singular value associated with the constant singular vector. This implies that in order for (26) to have an exact solution,  $\mathbf{c}_m^L$  must be orthogonal to the constant vector (see [18] for a complete discussion). The next theorem is one of the main results of this work and gives the conditions on the analytic metric terms so that the constraint (30) is satisfied.

**Theorem 3** *If the analytic metric terms used to populate  $\left[ \hat{\mathcal{J}}_\kappa \frac{\partial \hat{\xi}_l}{\partial x_m} \right]_{R_f}^{\hat{\Gamma}}$  are at most the degree of the weakest cubature rule involved in the nonconforming interface, then the constraints (30) are satisfied.*

*Proof* The proof follows from the accuracy of the interpolation operators and the associated cubature rules interacting at the nonconforming interface.

Thus far, the concentration has been on nonconforming faces. For nonconforming elements (i.e., elements that have at least one nonconforming face), on conforming faces the surface metric terms that appear in the discrete GCL (26) and (27) are taken as the surface metric terms of the adjoining face. The metric terms of the adjoining face are approximated using a standard approach, such as that of Vinokur and Yee [50] or Thomas and Lombard [49], and Theorem 2 of Ref. [18] guarantees that metric terms computed in this way satisfy the constraint (30).

#### 4 Nonlinearly stable schemes: Viscous Burgers' equation

The general  $h/p$ -nonconforming machinery presented in the previous section will be applied to the compressible Navier–Stokes equations in Section 5. However, in order for the resulting discretization to have the telescoping property, and therefore nonlinear stability, necessitates special nonlinear approximations that lead to this property. In this section, the required Hadamard derivative formulation is exemplified using the simple viscous Burgers' equation.

The viscous Burgers' equation and its canonically split form are

$$\frac{\partial \mathcal{U}}{\partial t} + \frac{\partial}{\partial x_1} \left( \frac{\mathcal{U}^2}{2} \right) = \frac{\partial^2 \mathcal{U}}{\partial x_1^2} \quad ; \quad \frac{\partial \mathcal{U}}{\partial t} + \frac{1}{3} \frac{\partial}{\partial x_1} (\mathcal{U}^2) + \frac{\mathcal{U}}{3} \frac{\partial \mathcal{U}}{\partial x_1} = \frac{\partial^2 \mathcal{U}}{\partial x_1^2}, \quad (32)$$

where, as in the convection-diffusion equation, the splitting is on the inviscid terms. Applying an energy analysis to the split form of (32) gives (for details see, for example, [9])

$$\frac{1}{2} \frac{d\|\mathcal{U}\|^2}{dt} + \oint_{\Gamma} \frac{\mathcal{U}^3}{3} n_{x_1} d\Gamma = \oint_{\Gamma} \mathcal{U} \frac{\partial \mathcal{U}}{\partial x_1} n_{x_1} d\Gamma - \int_{\Omega} \left( \frac{\partial \mathcal{U}}{\partial x_1} \right)^2 d\Omega, \quad \|\mathcal{U}\|^2 \equiv \int_{\Omega} \mathcal{U}^2 d\Omega. \quad (33)$$

The semi-discrete proof of stability that will be constructed shortly follows the continuous proof in a discrete sense such that when contracted by  $\mathbf{u}^T \mathbf{P}$ , i.e., the discrete analogue of multiplying by the solution and integrating in space, the result is the sum of spatial terms that telescope to the boundaries.

Ignoring the imposition of boundary conditions (i.e., SATs) and concentrating on a single element, then the discretization of (32) with SBP operators is given as

$$\frac{d\mathbf{u}}{dt} + \frac{1}{3} \mathbf{D}_{x_1} \text{diag}(\mathbf{u}) \mathbf{u} + \frac{1}{3} \text{diag}(\mathbf{u}) \mathbf{D}_{x_1} \mathbf{u} = \mathbf{D}_{x_1} \boldsymbol{\Theta}, \quad \boldsymbol{\Theta} \equiv \mathbf{D}_{x_1} \mathbf{u}. \quad (34)$$

Multiplying (34) by  $\mathbf{u}^T \mathbf{P}$  results in

$$\frac{1}{2} \frac{d\mathbf{u}^T \mathbf{P} \mathbf{u}}{dt} + \frac{1}{3} \left( \mathbf{u}^3(N) - \mathbf{u}^3(1) \right) = \mathbf{u}^T \mathbf{E}_{x_1} \mathbf{D}_{x_1} \mathbf{u} - \mathbf{u}^T \mathbf{D}_{x_1}^T \mathbf{P} \mathbf{D}_{x_1} \mathbf{u}, \quad (35)$$

where each term mimics the corresponding term in (33). Furthermore, Eq. (35) has the telescoping property, i.e., the remaining terms are at the boundaries.

Notice that the key to obtaining a telescoping semi-discrete form is the careful discretization of the inviscid terms (in this case using a canonical split form), whereas the viscous terms were directly discretized in strong conservation form.

The discrete inviscid terms in (34) can be recast using the Hadamard derivative formalism. The equivalence between the split form and the Hadamard derivative operators is given as follows

$$2\mathbf{D}_{x_1} \circ \mathbf{F}_{x_1}(\mathbf{u}, \mathbf{u}) \mathbf{1}_1 \quad \leftrightarrow \quad \frac{1}{3} \mathbf{D}_{x_1} \text{diag}(\mathbf{u}) \mathbf{u} + \frac{1}{3} \text{diag}(\mathbf{u}) \mathbf{D}_{x_1} \mathbf{u}. \quad (36)$$

Two components are used to construct the Hadamard derivative operator: first, an SBP derivative operator, and second a two-point flux function related to inviscid flux vector being discretely differentiated. The Hadamard derivative operator combines these two components such that two-point fluxes are constructed between the center point and all other points of dependency within the SBP stencil. The SBP telescoping property [25] results from precise local cancellation of spatial terms and can then be extended directly to nonlinear operators.

In the case of the Burgers' equation, the two-point flux function that results in an equivalence between the split form and the Hadamard derivative operator is [48, 9]

$$\mathbf{f}_{x_m}^{sc}(\mathbf{u}^{(i)}, \mathbf{u}^{(j)}) \equiv \frac{\left\{ \left( \mathbf{u}^{(i)} \right)^2 + \mathbf{u}^{(i)} \mathbf{u}^{(j)} + \left( \mathbf{u}^{(j)} \right)^2 \right\}}{6},$$

where  $\mathbf{u}^{(i)}$  and  $\mathbf{u}^{(j)}$  are the  $i^{\text{th}}$  and  $j^{\text{th}}$  components of  $\mathbf{u}$ . For the purpose of demonstration, a simple SBP operator constructed on the LGL nodes  $(-1, 0, 1)$  is

used:

$$\mathbf{D}_{x_1} = \begin{bmatrix} -\frac{3}{2} & 2 & -\frac{1}{2} \\ -\frac{1}{2} & 0 & \frac{1}{2} \\ \frac{1}{2} & -2 & \frac{3}{2} \end{bmatrix}.$$

The two argument Hadamard matrix flux,  $\mathbf{F}_{x_m}(\mathbf{u}, \mathbf{u})$  is given as

$$\mathbf{F}_{x_m}(\mathbf{u}, \mathbf{u}) = \begin{bmatrix} \frac{(\mathbf{u}^{(1)})^2}{2} & \frac{(\mathbf{u}^{(1)})^2 + \mathbf{u}^{(1)}\mathbf{u}^{(2)} + (\mathbf{u}^{(2)})^2}{6} & \frac{(\mathbf{u}^{(1)})^2 + \mathbf{u}^{(1)}\mathbf{u}^{(3)} + (\mathbf{u}^{(3)})^2}{6} \\ \frac{(\mathbf{u}^{(2)})^2 + \mathbf{u}^{(2)}\mathbf{u}^{(1)} + (\mathbf{u}^{(1)})^2}{6} & \frac{(\mathbf{u}^{(2)})^2}{2} & \frac{(\mathbf{u}^{(2)})^2 + \mathbf{u}^{(2)}\mathbf{u}^{(3)} + (\mathbf{u}^{(3)})^2}{6} \\ \frac{(\mathbf{u}^{(3)})^2 + \mathbf{u}^{(3)}\mathbf{u}^{(1)} + (\mathbf{u}^{(1)})^2}{6} & \frac{(\mathbf{u}^{(3)})^2 + \mathbf{u}^{(3)}\mathbf{u}^{(2)} + (\mathbf{u}^{(2)})^2}{6} & \frac{(\mathbf{u}^{(3)})^2}{2} \end{bmatrix}.$$

Thus,

$$\mathbf{D}_{x_1} \circ \mathbf{F}_{x_m}(\mathbf{u}, \mathbf{u}) \mathbf{1} = \begin{bmatrix} -\frac{3}{2} \frac{(\mathbf{u}^{(1)})^2}{2} & 2 \frac{(\mathbf{u}^{(1)})^2 + \mathbf{u}^{(1)}\mathbf{u}^{(2)} + (\mathbf{u}^{(2)})^2}{6} & -\frac{1}{2} \frac{(\mathbf{u}^{(1)})^2 + \mathbf{u}^{(1)}\mathbf{u}^{(3)} + (\mathbf{u}^{(3)})^2}{6} \\ -\frac{1}{2} \frac{(\mathbf{u}^{(2)})^2 + \mathbf{u}^{(2)}\mathbf{u}^{(1)} + (\mathbf{u}^{(1)})^2}{6} & 0 & \frac{1}{2} \frac{(\mathbf{u}^{(2)})^2 + \mathbf{u}^{(2)}\mathbf{u}^{(3)} + (\mathbf{u}^{(3)})^2}{6} \\ \frac{1}{2} \frac{(\mathbf{u}^{(3)})^2 + \mathbf{u}^{(3)}\mathbf{u}^{(1)} + (\mathbf{u}^{(1)})^2}{6} & -2 \frac{(\mathbf{u}^{(3)})^2 + \mathbf{u}^{(3)}\mathbf{u}^{(2)} + (\mathbf{u}^{(2)})^2}{6} & \frac{3}{2} \frac{(\mathbf{u}^{(3)})^2}{2} \end{bmatrix} \begin{bmatrix} 1 \\ 1 \\ 1 \end{bmatrix}.$$

The equivalence between the two approaches can be determined via inspection.

The general notation necessary for discretizing the inviscid fluxes of the compressible Navier–Stokes equations is now detailed. Consider the discretization of the derivative of a flux vector  $\mathcal{F}_{x_m}$  in the  $x_m$  Cartesian direction. As for the Burgers' equation, the key components are an SBP matrix difference operator,  $\mathbf{D}_{x_m}$ , and a two argument matrix flux function,  $\mathbf{F}_{x_m}(\mathbf{u}_\kappa, \mathbf{u}_r)$ , which is constructed from diagonal matrices and is defined block-wise as

$$(\mathbf{F}_{x_m}(\mathbf{u}_\kappa, \mathbf{u}_r))(e(i-1)+1 : ei, e(j-1)+1 : ej) \equiv \text{diag} \left( \mathbf{f}_{x_m}^{sc} \left( \mathbf{u}_\kappa^{(i)}, \mathbf{u}_r^{(j)} \right) \right),$$

$$\mathbf{u}_\kappa^{(i)} \equiv \mathbf{u}_\kappa(e(i-1)+1 : ei), \quad \mathbf{u}_r^{(j)} \equiv \mathbf{u}_r(e(j-1)+1 : ej),$$

$$i = 1 \dots, N_\kappa^3, \quad j = 1, \dots, N_r^3,$$

where  $e$  is the number of equations in the system of PDEs. In the context of the compressible Navier–Stokes equations  $e = 5$  and the two argument matrix flux function is of size  $(eN_\kappa^3) \times (eN_r^3)$ , where  $eN_\kappa^3$  and  $eN_r^3$  are the total number of entries in the vectors  $\mathbf{u}_\kappa$  and  $\mathbf{u}_r$  corresponding the solution variables in elements  $\kappa$  and  $r$ , respectively. Therefore,  $\mathbf{u}_\kappa^{(i)}$  is the vector of the  $e$  solution variables evaluated at the  $i^{\text{th}}$  node. The vectors  $\mathbf{f}_{x_m}^{sc}(\mathbf{u}_\kappa^{(i)}, \mathbf{u}_r^{(j)})$  are constructed from two-point flux functions that are symmetric in their arguments,  $(\mathbf{u}_\kappa^{(i)}, \mathbf{u}_r^{(j)})$ , and consistent, i.e.,

$$\mathbf{f}_{x_m}^{sc}(\mathbf{u}_\kappa^{(i)}, \mathbf{u}_r^{(j)}) = \mathbf{f}_{x_m}^{sc}(\mathbf{u}_r^{(j)}, \mathbf{u}_\kappa^{(i)}), \quad \mathbf{f}_{x_m}^{sc}(\mathbf{u}_\kappa^{(i)}, \mathbf{u}_\kappa^{(i)}) = \mathcal{F}_{x_m}(\mathbf{u}_\kappa^{(i)}),$$

where  $\mathcal{F}_{x_m}$  is the inviscid flux vector in the  $x_m$  Cartesian direction. With the notation defined, the Hadamard differentiation operator for the inviscid flux,  $\frac{\partial \mathcal{F}_{x_m}}{\partial x_m}$ , is constructed as

$$2D_{x_m} \circ \mathbf{F}_{x_m}(\mathbf{q}_\kappa, \mathbf{q}_\kappa) \mathbf{1}_\kappa \approx \frac{\partial \mathcal{F}_{x_m}}{\partial x_m}(\mathbf{x}^\kappa),$$

where  $\mathbf{x}^\kappa$  is the vector of vectors containing the nodal coordinates. The resulting approximation has equivalent order properties as constructing an approximation to the derivative of the flux vector directly using an SBP operator  $D_{x_m}$  (see Theorem 1 in Crean *et al.* [12]).

## 5 Application to the compressible Navier–Stokes equations

Herein, the nonconforming algorithm presented in Section 3 is combined with the mechanics presented in Section 4 to construct an entropy conservative discretization of the compressible Navier–Stokes equations for arbitrary  $h/p$ -nonconforming meshes. First, the continuous equations and entropy analysis are reviewed in Section 5.1. Second, in Section 5.2, the semi-discrete algorithm is presented and analyzed.

### 5.1 Review of the continuous entropy analysis

The entropy stable algorithm is constructed by discretizing the skew-symmetric form of the compressible Navier–Stokes equations, with the viscous flux recast in terms of entropy variables. This form of the equations is given as

$$\begin{aligned} \mathcal{J}_\kappa \frac{\partial \mathcal{Q}_\kappa}{\partial t} + \frac{1}{2} \sum_{l,m=1}^3 \left( \frac{\partial}{\partial \xi_l} \left( \mathcal{J}_\kappa \frac{\partial \xi_l}{\partial x_m} \mathcal{F}_{x_m}^I \right) + \mathcal{J}_\kappa \frac{\partial \xi_l}{\partial x_m} \frac{\partial \mathcal{F}_{x_m}^I}{\partial \xi_l} \right) \\ - \frac{1}{2} \sum_{l,m=1}^3 \mathcal{F}_{x_m}^I \frac{\partial}{\partial \xi_l} \left( \mathcal{J}_\kappa \frac{\partial \xi_l}{\partial x_m} \right) = \sum_{l,a=1}^3 \frac{\partial}{\partial \xi_l} \left( \hat{c}_{l,a} \frac{\partial \mathcal{W}}{\partial \xi_a} \right), \end{aligned} \quad (37)$$

where the last set of terms on the left-hand side are zero by the GCL relations (6). Furthermore,

$$\hat{c}_{l,a} = \mathcal{J}_\kappa \frac{\partial \xi_l}{\partial x_m} \sum_{m,j=1}^3 c_{m,j} \frac{\partial \xi_a}{\partial x_j}, \quad (38)$$

$\mathcal{Q}$  is the vector of conserved variables, and  $\mathcal{F}_{x_m}^I$  is the inviscid flux vector in the  $x_m$  direction. The vector of conserved variables is given by

$$\mathcal{Q} = [\rho, \rho \mathcal{U}_1, \rho \mathcal{U}_2, \rho \mathcal{U}_3, \rho \mathcal{E}]^\top,$$

where  $\rho$  denotes the density,  $\mathcal{U} = [\mathcal{U}_1, \mathcal{U}_2, \mathcal{U}_3]^\top$  is the velocity vector, and  $\mathcal{E}$  is the specific total energy. The inviscid fluxes are given as

$$\begin{aligned} \mathcal{F}_{x_m}^I = [\rho \mathcal{U}_m, \rho \mathcal{U}_m \mathcal{U}_1 + \delta_{m,1} \mathcal{P}, \rho \mathcal{U}_m \mathcal{U}_2 + \delta_{m,2} \mathcal{P}, \\ \rho \mathcal{U}_m \mathcal{U}_3 + \delta_{m,3} \mathcal{P}, \rho \mathcal{U}_m \mathcal{H}]^\top, \end{aligned}$$

where  $\mathcal{P}$  is the pressure,  $\mathcal{H}$  is the specific total enthalpy and  $\delta_{i,j}$  is the Kronecker delta.

The necessary constituent relations are

$$\mathcal{H} = c_p \mathcal{T} + \frac{1}{2} \mathbf{U}^T \mathbf{U}, \quad \mathcal{P} = \rho R \mathcal{T}, \quad R = \frac{R_u}{M_w},$$

where  $\mathcal{T}$  is the temperature,  $R_u$  is the universal gas constant,  $M_w$  is the molecular weight of the gas, and  $c_p$  is the specific heat capacity at constant pressure. Finally, the specific thermodynamic entropy is given as

$$s = \frac{R}{\gamma - 1} \log \left( \frac{\mathcal{T}}{\mathcal{T}_\infty} \right) - R \log \left( \frac{\rho}{\rho_\infty} \right), \quad \gamma = \frac{c_p}{c_p - R},$$

where  $\mathcal{T}_\infty$  and  $\rho_\infty$  are the reference temperature and density, respectively.

The viscous fluxes,  $\mathcal{F}_{x_m}^V$ , have been recast in terms of the entropy variables,  $\mathcal{W} \equiv \partial \mathcal{S} / \partial \mathcal{Q}$ , where  $\mathcal{S}$  is the entropy function  $\mathcal{S} \equiv -\rho s$ :

$$\mathcal{F}_{x_m}^V = \sum_{j=1}^3 C_{m,j} \frac{\partial \mathcal{W}}{\partial x_j}. \quad (39)$$

The viscous fluxes written in components are given as

$$\mathcal{F}_{x_m}^V = \left[ 0, \tau_{1,m}, \tau_{2,m}, \tau_{3,m}, \sum_{i=1}^3 \tau_{i,m} \mathcal{U}_i - \kappa \frac{\partial \mathcal{T}}{\partial x_m} \right]^T, \quad (40)$$

and the viscous stresses are defined as

$$\tau_{i,j} = \mu \left( \frac{\partial \mathcal{U}_i}{\partial x_j} + \frac{\partial \mathcal{U}_j}{\partial x_i} - \delta_{i,j} \frac{2}{3} \sum_{n=1}^3 \frac{\partial \mathcal{U}_n}{\partial x_n} \right), \quad (41)$$

where  $\mu(T)$  is the dynamic viscosity and  $\kappa(T)$  is the thermal conductivity (not to be confused with the choice of parameter for element numbering).

The compressible Navier–Stokes equations have a convex extension, that when integrated over the physical domain,  $\Omega$ , depends only on the boundary data and negative semi-definite dissipation terms. This convex extension depends on an entropy function,  $\mathcal{S}$ , and it is used to prove the stability in the  $L^2$  norm. Here, a brief review of the entropy stability analysis is given. A detailed presentation is available, for instance, in [13, 43, 9].

Under the assumption that the entropy function  $\mathcal{S}$  is convex, which is guaranteed if  $\rho, \mathcal{T} > 0$ , then the vector of entropy variables,  $\mathcal{W}$ , simultaneously contracts all of the inviscid flux as follows:

$$\mathcal{W}^T \frac{\partial \mathcal{F}_{x_m}^I}{\partial \xi_l} = \frac{\partial \mathcal{S}}{\partial \mathcal{Q}} \frac{\partial \mathcal{F}_{x_m}^I}{\partial \mathcal{Q}} \frac{\partial \mathcal{Q}}{\partial \xi_l} = \frac{\partial \mathcal{F}_{x_m}}{\partial \mathcal{Q}} \frac{\partial \mathcal{F}_{x_m}^I}{\partial \mathcal{Q}}, \quad l, m = 1, 2, 3, \quad (42)$$

where  $\mathcal{F}_{x_m}$  is the entropy flux in the  $x_m$  direction.

The entropy stability analysis proceeds by first multiplying (contracting) Eq. (37) by the transpose of the entropy variables,  $\mathbf{W}^T$ ,

$$\begin{aligned} & \overbrace{\mathcal{J}_\kappa \mathbf{W}^T \frac{\partial \mathcal{Q}_\kappa}{\partial t}}^I + \frac{1}{2} \sum_{l,m=1}^3 \left( \overbrace{\mathbf{W}^T \frac{\partial}{\partial \xi_l} \left( \mathcal{J}_\kappa \frac{\partial \xi_l}{\partial x_m} \mathcal{F}_{x_m}^I \right)}^{II} + \overbrace{\mathcal{J}_\kappa \frac{\partial \xi_l}{\partial x_m} \mathbf{W}^T \frac{\partial \mathcal{F}_{x_m}^I}{\partial \xi_l}}^{III} \right) = \\ & \sum_{l,a=1}^3 \overbrace{\mathbf{W}^T \frac{\partial}{\partial \xi_l} \left( \hat{c}_{l,a} \frac{\partial \mathcal{W}}{\partial \xi_a} \right)}^{IV}. \end{aligned} \quad (43)$$

With the help of Eq. (42) and the product rule, the terms  $I$ – $IV$  are now simplified:

$$I \equiv \mathcal{J}_\kappa \mathbf{W}^T \frac{\partial \mathcal{Q}_\kappa}{\partial t} = \mathcal{J}_\kappa \frac{\partial \mathcal{S}}{\partial \mathcal{Q}} \frac{\partial \mathcal{Q}_\kappa}{\partial t} = \mathcal{J}_\kappa \frac{\partial \mathcal{S}_\kappa}{\partial t}, \quad (44)$$

$$\begin{aligned} II \equiv \mathbf{W}^T \frac{\partial}{\partial \xi_l} \left( \mathcal{J}_\kappa \frac{\partial \xi_l}{\partial x_m} \mathcal{F}_{x_m}^I \right) &= \mathcal{J}_\kappa \frac{\partial \xi_l}{\partial x_m} \mathbf{W}^T \frac{\partial \mathcal{F}_{x_m}^I}{\partial \xi_l} + \mathbf{W}^T \mathcal{F}_{x_m}^I \frac{\partial}{\partial \xi_l} \left( \mathcal{J}_\kappa \frac{\partial \xi_l}{\partial x_m} \right) \\ &= \mathcal{J}_\kappa \frac{\partial \xi_l}{\partial x_m} \frac{\partial \mathcal{F}_{x_m}^I}{\partial \xi_l} + \mathbf{W}^T \mathcal{F}_{x_m}^I \frac{\partial}{\partial \xi_l} \left( \mathcal{J}_\kappa \frac{\partial \xi_l}{\partial x_m} \right), \end{aligned} \quad (45)$$

$$III \equiv \mathcal{J}_\kappa \frac{\partial \xi_l}{\partial x_m} \mathbf{W}^T \frac{\partial \mathcal{F}_{x_m}^I}{\partial \xi_l} = \mathcal{J}_\kappa \frac{\partial \xi_l}{\partial x_m} \frac{\partial \mathcal{F}_{x_m}^I}{\partial \xi_l}, \quad (46)$$

$$IV \equiv \mathbf{W}^T \frac{\partial}{\partial \xi_l} \left( \hat{c}_{l,a} \frac{\partial \mathcal{W}}{\partial \xi_a} \right) = \frac{\partial}{\partial \xi_l} \left( \mathbf{W}^T \hat{c}_{l,a} \frac{\partial \mathcal{W}}{\partial \xi_a} \right) - \frac{\partial \mathbf{W}^T}{\partial \xi_l} \hat{c}_{l,a} \frac{\partial \mathcal{W}}{\partial \xi_a}. \quad (47)$$

Substituting Eq. (44) through (47) into (43) results in

$$\begin{aligned} & \mathcal{J}_\kappa \frac{\partial \mathcal{S}_\kappa}{\partial t} + \sum_{l,m=1}^3 \mathcal{J}_\kappa \frac{\partial \xi_l}{\partial x_m} \frac{\partial \mathcal{F}_{x_m}^I}{\partial \xi_l} + \frac{\mathbf{W}^T}{2} \sum_{m=1}^3 \mathcal{F}_{x_m}^I \sum_{l=1}^3 \frac{\partial}{\partial \xi_l} \left( \mathcal{J}_\kappa \frac{\partial \xi_l}{\partial x_m} \right) \overset{0 \text{ via GCL (6)}}{=} \\ & \sum_{l,a=1}^3 \left\{ \frac{\partial}{\partial \xi_l} \left( \mathbf{W}^T \hat{c}_{l,a} \frac{\partial \mathcal{W}}{\partial \xi_a} \right) - \frac{\partial \mathbf{W}^T}{\partial \xi_l} \hat{c}_{l,a} \frac{\partial \mathcal{W}}{\partial \xi_a} \right\}. \end{aligned} \quad (48)$$

Bringing the metric terms within the derivative on the term  $\mathcal{J}_\kappa \frac{\partial \xi_l}{\partial x_m} \frac{\partial \mathcal{F}_{x_m}^I}{\partial \xi_l}$  and using the product rule results in

$$\begin{aligned} & \mathcal{J}_\kappa \frac{\partial \mathcal{S}_\kappa}{\partial t} + \sum_{l,m=1}^3 \frac{\partial}{\partial \xi_l} \left( \mathcal{J}_\kappa \frac{\partial \xi_l}{\partial x_m} \mathcal{F}_{x_m}^I \right) - \sum_{m=1}^3 \mathcal{F}_{x_m}^I \sum_{l=1}^3 \frac{\partial}{\partial \xi_l} \left( \mathcal{J}_\kappa \frac{\partial \xi_l}{\partial x_m} \right) \overset{0 \text{ via GCL (6)}}{=} \\ & \sum_{l,a=1}^3 \left\{ \frac{\partial}{\partial \xi_l} \left( \mathbf{W}^T \hat{c}_{l,a} \frac{\partial \mathcal{W}}{\partial \xi_a} \right) - \frac{\partial \mathbf{W}^T}{\partial \xi_l} \hat{c}_{l,a} \frac{\partial \mathcal{W}}{\partial \xi_a} \right\}. \end{aligned} \quad (49)$$

Rearranging Eq. (49) and expanding the dissipation term yields

$$\begin{aligned} \mathcal{J}_\kappa \frac{\partial \mathcal{S}_\kappa}{\partial t} &= \sum_{l=1}^3 \frac{\partial}{\partial \xi_l} \left( - \sum_{m=1}^3 \mathcal{J}_\kappa \frac{\partial \xi_l}{\partial x_m} \mathcal{F}_{x_m} + \sum_{a=1}^3 \left( \mathbf{w}^T \hat{\mathbf{C}}_{l,a} \frac{\partial \mathcal{W}}{\partial \xi_a} \right) \right) \\ &- \begin{bmatrix} \frac{\partial \mathcal{W}}{\partial \xi_1} \\ \frac{\partial \mathcal{W}}{\partial \xi_2} \\ \frac{\partial \mathcal{W}}{\partial \xi_3} \end{bmatrix}^T \underbrace{\begin{bmatrix} \hat{\mathbf{C}}_{1,1} & \hat{\mathbf{C}}_{1,2} & \hat{\mathbf{C}}_{1,3} \\ \hat{\mathbf{C}}_{1,2}^T & \hat{\mathbf{C}}_{2,2} & \hat{\mathbf{C}}_{2,3} \\ \hat{\mathbf{C}}_{1,3}^T & \hat{\mathbf{C}}_{2,3}^T & \hat{\mathbf{C}}_{3,3} \end{bmatrix}}_{\equiv \hat{\mathbf{C}}} \underbrace{\begin{bmatrix} \frac{\partial \mathcal{W}}{\partial \xi_1} \\ \frac{\partial \mathcal{W}}{\partial \xi_2} \\ \frac{\partial \mathcal{W}}{\partial \xi_3} \end{bmatrix}}_{\equiv \hat{\mathbf{w}}}, \end{aligned} \quad (50)$$

where the matrix  $\hat{\mathbf{C}}$  is symmetric semi-definite (see [23] for details).

Integrating Eq. (50) in space and using integration by parts gives

$$\int_{\hat{\Omega}_\kappa} \mathcal{J}_\kappa \frac{\partial \mathcal{S}_\kappa}{\partial t} d\hat{\Omega} \leq \sum_{l=1}^3 \oint_{\hat{\Gamma}_\kappa} \left( - \sum_{m=1}^3 \mathcal{J}_\kappa \frac{\partial \xi_l}{\partial x_m} \mathcal{F}_{x_m} + \sum_{a=1}^3 \left( \mathbf{w}^T \hat{\mathbf{C}}_{l,a} \frac{\partial \mathcal{W}}{\partial \xi_a} \right) \right) n_{\xi_l} d\hat{\Gamma}. \quad (51)$$

An  $L^2$  bound on the solution is derived from inequality (51) by integrating in time and assuming 1) nonlinearly well-posed boundary and initial conditions, and 2) positivity of temperature and density. Then, the result can be turned into a bound on the solution in terms of the data of the problem [13, 43].

## 5.2 An $h/p$ -nonconforming algorithm

The skew-symmetrically split form of the compressible Navier–Stokes equations (37) is discretized by combining the macro element SBP operator in Section 3.2 with the nonlinear mechanics presented in Section 4. Thus, the discretization of (37) over the macro element is given as

$$\begin{aligned} & \int \frac{d\tilde{\mathbf{q}}}{dt} + \sum_{l,m=1}^3 \tilde{\mathbf{D}}_{l,m} \circ \mathbf{F}_{x_m}(\tilde{\mathbf{q}}, \tilde{\mathbf{q}}) \tilde{\mathbf{1}} \\ & - \frac{1}{2} \sum_{l,m=1}^3 \text{diag}(\mathbf{f}_{x_m}^I) \tilde{\mathbf{D}}_{\hat{\xi}_l} \left[ \hat{\mathcal{J}}_\kappa \frac{\partial \hat{\xi}_l}{\partial x_m} \right] \tilde{\mathbf{1}} = \sum_{l,a=1}^3 \tilde{\mathbf{D}}_{\hat{\xi}_l} [\hat{\mathbf{C}}_{l,a}] \tilde{\mathbf{D}}_{\hat{\xi}_a} \tilde{\mathbf{w}}, \end{aligned} \quad (52)$$

$$\tilde{\mathbf{q}} \equiv [\mathbf{q}_L^T, \mathbf{q}_{R_1}^T, \dots, \mathbf{q}_{R_4}^T]^T, \quad \tilde{\mathbf{w}} \equiv [\mathbf{w}_L^T, \mathbf{w}_{R_1}^T, \dots, \mathbf{w}_{R_4}^T]^T,$$

where  $\mathbf{f}_{x_m}^I$  is a vector of vectors constructed by evaluating  $\mathcal{F}_{x_m}^I$  at the mesh nodes. Note that the factor of  $\frac{1}{2}$  on the skew-symmetric inviscid volume terms has been absorbed as a result of using the nonlinear operator, e.g.,  $2\mathbf{D}_{\hat{\xi}_l} \circ \mathbf{F}_{x_m}(\mathbf{q}_\kappa, \mathbf{q}_\kappa) \mathbf{1}_\kappa \approx \frac{\partial \mathcal{F}_{x_m}}{\partial \xi_l}(\boldsymbol{\xi}^\kappa)$ . Furthermore, the flux function matrix,  $\mathbf{F}_{x_m}(\tilde{\mathbf{q}}, \tilde{\mathbf{q}})$ , is constructed using a two-point flux function,  $\mathbf{f}_{x_m}^{sc}(\tilde{\mathbf{q}}^{(i)}, \tilde{\mathbf{q}}^{(j)})$ , that satisfies the Tadmor's shuffle condition [48]

$$(\tilde{\mathbf{w}}^{(i)} - \tilde{\mathbf{w}}^{(j)})^T \mathbf{f}_{x_m}^{sc}(\tilde{\mathbf{q}}^{(i)}, \tilde{\mathbf{q}}^{(j)}) = \tilde{\psi}_{x_m}^{(i)} - \tilde{\psi}_{x_m}^{(j)}. \quad (53)$$



The  $\tilde{D}_{l,m}$  operators are constructed from the scalar conservation law operators developed in Section (3) by tensoring them with an identity matrix,  $\mathbf{I}_5$ , to accommodate the system of five equations. For example,

$$D_{\xi_1}^L \equiv \bar{D}_{\xi_1} \otimes \mathbf{I}_5, \quad \bar{D}_{\xi_1}^L \equiv \frac{2}{\Delta_1^L} D_L^{(1D)} \otimes \mathbf{I}_L \otimes \mathbf{I}_L.$$

Similar to the linear stability, entropy stability necessitates that the last set of terms on the left-hand side of (52) be zero and leads to the same set of discrete GCL conditions.

The semi-discrete entropy analysis follows the continuous analysis in a one-to-one fashion. In order to simplify the derivation, the following matrices are introduced:

$$\tilde{D}_m \equiv \sum_{l=1}^3 \tilde{D}_{l,m}, \quad \tilde{Q}_m \equiv \tilde{P} \tilde{D}_m, \quad \tilde{E}_m \equiv \tilde{Q}_m + \tilde{Q}_m^T.$$

Assuming that the discrete GCL conditions are satisfied, (52) becomes

$$\int \frac{d\tilde{q}}{dt} + \sum_{m=1}^3 \tilde{D}_m \circ F_{x_m}(\tilde{q}, \tilde{q}) \tilde{\mathbf{I}} = \sum_{l,a=1}^3 \tilde{D}_{\xi_l} [\hat{C}_{l,a}] \tilde{D}_{\xi_a} \tilde{w}. \quad (54)$$

Multiplying Eq. (54) by  $\tilde{w}^T \tilde{P}$  (the discrete analogue of multiplying by  $\mathcal{W}^T$  and integrating over the domain) yields

$$\int \tilde{w}^T \tilde{P} \frac{d\tilde{q}}{dt} + \sum_{m=1}^3 \tilde{w} \tilde{Q}_m \circ F_{x_m}(\tilde{q}, \tilde{q}) \tilde{\mathbf{I}} = \sum_{l,a=1}^3 \tilde{w}^T \tilde{Q}_{\xi_l} [\hat{C}_{l,a}] \tilde{D}_{\xi_a} \tilde{w}. \quad (55)$$

Taking the transpose of one half of the volume term on the left-hand side of Eq. (55), using the SBP property  $\mathbf{Q} = -\mathbf{Q}^T + \mathbf{E}$ , and the symmetry of the two-point flux function matrix, results in

$$\begin{aligned} \int \tilde{w}^T \tilde{P} \frac{d\tilde{q}}{dt} + \frac{1}{2} \sum_{m=1}^3 \left( \tilde{w} \tilde{Q}_m \circ F_{x_m}(\tilde{q}, \tilde{q}) \tilde{\mathbf{I}} - \tilde{\mathbf{I}}^T \tilde{Q}_m \circ F_{x_m}(\tilde{q}, \tilde{q})^T \tilde{w} \right. \\ \left. + \tilde{\mathbf{I}}^T \tilde{E}_m \circ F_{x_m}(\tilde{q}, \tilde{q})^T \tilde{w} \right) = \\ \sum_{l,a=1}^3 \tilde{w}^T \tilde{E}_{\xi_l} [\hat{C}_{l,a}] \tilde{D}_{\xi_a} \tilde{w} - \sum_{l,a=1}^3 \tilde{w}^T \tilde{D}_{\xi_l}^T \tilde{P} [\hat{C}_{l,a}] \tilde{D}_{\xi_a} \tilde{w}. \end{aligned} \quad (56)$$

To further reduce the left-hand side terms requires the following theorem (this is Theorem 8 in [16] and the proof is given in Appendix D of that document):

**Theorem 4** Consider the matrix of  $\bar{A}$  of size  $N_\kappa \times N_r$  with a tensor extension  $\mathbf{A} \equiv \bar{A} \otimes \mathbf{I}_5$ , and a two argument matrix flux function  $F_{x_m}(\mathbf{q}_\kappa, \mathbf{q}_r)$  constructed from the two-point flux function  $\mathbf{f}_{x_m}^{sc}(\mathbf{q}_\kappa^{(i)}, \mathbf{q}_r^{(j)})$  that satisfies the Tadmor's shuffle condition

$$\left( \mathbf{w}_\kappa^{(i)} - \mathbf{w}_r^{(j)} \right)^T \mathbf{f}_{x_m}^{sc}(\mathbf{q}_\kappa^{(i)}, \mathbf{q}_r^{(j)}) = (\psi_{x_m}^\kappa)^{(i)} - (\psi_{x_m}^r)^{(j)}$$

and is symmetric, i.e.,  $\mathbf{f}_{x_m}^{sc}(\mathbf{q}_\kappa^{(i)}, \mathbf{q}_r^{(j)}) = \mathbf{f}_{x_m}^{sc}(\mathbf{q}_r^{(j)}, \mathbf{q}_\kappa^{(i)})$ , then

$$\mathbf{w}_T(\mathbf{A}) \circ F_{x_m}(\mathbf{q}_\kappa, \mathbf{q}_r) \mathbf{1}_r - \mathbf{1}_\kappa^T \mathbf{A} \circ F_{x_m}(\mathbf{q}_\kappa, \mathbf{q}_r) \mathbf{w}_r = (\psi_{x_m}^\kappa)^T \bar{\mathbf{A}} \mathbf{1}_r - \mathbf{1}_\kappa^T \bar{\mathbf{A}} \psi_{x_m}^r.$$

Applying Theorem 4 to the volume terms on the left-hand side of Eq. (56) yields

$$\begin{aligned} \int \tilde{\mathbf{w}}^T \tilde{\mathbf{P}} \frac{d\tilde{\mathbf{q}}}{dt} + \frac{1}{2} \sum_{m=1}^3 \left\{ \left( \widetilde{\psi_{x_m}} \right)^T \bar{\mathbf{Q}}_m \bar{\mathbf{I}} - \bar{\mathbf{I}}^T \bar{\mathbf{Q}}_m \widetilde{\psi_{x_m}} + \tilde{\mathbf{I}}^T \tilde{\mathbf{E}}_m \circ \mathbf{F}_{x_m}(\tilde{\mathbf{q}}, \tilde{\mathbf{q}})^T \tilde{\mathbf{w}} \right\} = \\ \sum_{l,a=1}^3 \tilde{\mathbf{w}}^T \tilde{\mathbf{E}}_{\hat{\xi}_l} \left[ \hat{\mathbf{C}}_{l,a} \right] \tilde{\mathbf{D}}_{\hat{\xi}_a} \tilde{\mathbf{w}} - \sum_{l,a=1}^3 \tilde{\mathbf{w}}^T \tilde{\mathbf{D}}_{\hat{\xi}_l}^T \tilde{\mathbf{P}} \left[ \hat{\mathbf{C}}_{l,a} \right] \tilde{\mathbf{D}}_{\hat{\xi}_a} \tilde{\mathbf{w}}. \end{aligned} \quad (57)$$

The term  $\bar{\mathbf{Q}}_m \bar{\mathbf{I}}$  is zero by the discrete GCL conditions and the consistency of the derivative operator ( $\mathbf{D}\mathbf{1} = \mathbf{0}$ ) and for the same reasons  $\bar{\mathbf{I}}^T \bar{\mathbf{Q}}_m = \bar{\mathbf{I}}^T \bar{\mathbf{E}}_m$ . Therefore, after some rearrangements Eq. (58) reduces to

$$\begin{aligned} \int \tilde{\mathbf{w}}^T \tilde{\mathbf{P}} \frac{d\tilde{\mathbf{q}}}{dt} = -\frac{1}{2} \sum_{m=1}^3 \left\{ -\bar{\mathbf{I}}^T \bar{\mathbf{E}}_m \widetilde{\psi_{x_m}} + \tilde{\mathbf{I}}^T \tilde{\mathbf{E}}_m \circ \mathbf{F}_{x_m}(\tilde{\mathbf{q}}, \tilde{\mathbf{q}})^T \tilde{\mathbf{w}} \right\} \\ + \sum_{l,a=1}^3 \tilde{\mathbf{w}}^T \tilde{\mathbf{E}}_{\hat{\xi}_l} \left[ \hat{\mathbf{C}}_{l,a} \right] \tilde{\mathbf{D}}_{\hat{\xi}_a} \tilde{\mathbf{w}} - \sum_{l,a=1}^3 \tilde{\mathbf{w}}^T \tilde{\mathbf{D}}_{\hat{\xi}_l}^T \tilde{\mathbf{P}} \left[ \hat{\mathbf{C}}_{l,a} \right] \tilde{\mathbf{D}}_{\hat{\xi}_a} \tilde{\mathbf{w}}. \end{aligned} \quad (58)$$

The right-hand side of (58) contains surface terms (those constructed from the  $\mathbf{E}$  matrices) and viscous dissipation terms (the last set of terms). The surface terms can be decomposed into the contributions of the separate surfaces of the element (node-wise). The entropy conservation of the algorithm follows immediately for periodic problems because these terms would cancel out with the contributions from the coupling SATs. For general boundary conditions, appropriate SATs need to be constructed so that an entropy inequality or equality is attained (see, for example, [37, 44, 14]).

## 6 Interface dissipation and boundary SATs

In order to render the entropy conservative scheme entropy stable, interface dissipation is added. The numerical dissipation added for the inviscid SATs (i.e., added to the right-hand side of the discretization) is motivated by a Roe approximate Riemann solver (for a detailed discussion see [4, 36, 18, 16]). The inviscid dissipation for element  $L$  is given as

$$diss_L \equiv - \left( \mathbf{P}^L \right)^{-1} \mathbf{R}_L^T \mathbf{P}_{\perp \hat{\xi}_1}^L \left\{ \sum_{f=1}^4 \mathbf{l}_{R_f \text{ to } L} \left| \frac{\partial \mathcal{F}_{\hat{\xi}_1}^I}{\partial \mathcal{W}} \right|_{R_f} \left( \mathbf{l}_{L \text{ to } R_f} \mathbf{R}_L \mathbf{w}_L - \mathbf{R}_{R_f} \mathbf{w}_{R_f} \right) \right\}, \quad (59)$$

where

$$\begin{aligned} \mathbf{R}_L &\equiv \left( \mathbf{e}_{N_1}^L \right)^T \otimes \mathbf{l}_L \otimes \mathbf{l}_L \otimes \mathbf{l}_5, \\ \mathbf{P}_{\perp \hat{\xi}_1}^L &\equiv \frac{\Delta_2^L \Delta_3^L}{4} \mathbf{P}_L^{(1D)} \otimes \mathbf{P}_L^{(1D)} \otimes \mathbf{l}_5, \\ \mathbf{l}_{R_f \text{ to } L} &\equiv \mathbf{l}_{R_f \text{ to } L}^2 \otimes \mathbf{l}_{R_f \text{ to } L}^3 \otimes \mathbf{l}_5, \\ \mathbf{l}_{L \text{ to } R_f} &\equiv \mathbf{l}_{L \text{ to } R_f}^2 \otimes \mathbf{l}_{L \text{ to } R_f}^3 \otimes \mathbf{l}_5, \\ \mathbf{R}_{R_f} &\equiv \left( \mathbf{e}_{1_1}^{R_f} \right)^T \otimes \mathbf{l}_{R_f} \otimes \mathbf{l}_{R_f} \otimes \mathbf{l}_5. \end{aligned}$$

The inviscid dissipation term for the  $R_f$  element is constructed as

$$diss_{R_f} \equiv - \left( P_f^R \right)^{-1} R_{R_f}^T P_{\perp \xi_1}^{R_f} \left| \frac{\partial \mathcal{F}^I}{\partial \mathcal{W}} \right|_{R_f} \left( R_{R_f} \mathbf{w}_{R_f} - I_{LtoR_f} R_L \mathbf{w}_L \right), \quad (60)$$

where

$$\left| \frac{\partial \mathcal{F}^I}{\partial \mathcal{W}} \right| \equiv Y |\Lambda| Y^T.$$

The matrices  $Y$  and  $\Lambda$  are block diagonal matrices constructed by assembling the point-wise  $5 \times 5$  matrices obtained from the decomposition of the Jacobian matrix of  $\mathcal{F}$  with respect to  $\mathcal{W}$  and evaluated at the Roe-averaged of two states. In particular,  $\left| \frac{\partial \mathcal{F}^I}{\partial \mathcal{W}} \right|_{R_f}$  is constructed from the Roe averaged states of  $I_{LtoR_{qL}}$  and  $q_{R_f}$ .

Next, a theorem on the accuracy, stability, element-wise conservation, and free-stream preservation of the inviscid dissipation term is presented.

**Theorem 5** *The dissipation terms (59) and (60) are of order  $\min(p_L, p_{R_1}, \dots, p_{R_4}) + 3$ , and lead to an entropy stable inviscid scheme and have no impact on element-wise conservation or free-stream preservation.*

*Proof* The proofs are similar to those in Ref. [18, 16] and are omitted for brevity.

The viscous interface dissipation terms (interior penalty terms) take the following form:

$$I_P^L \equiv - \left( P^L \right)^{-1} R_L^T P_{\perp \xi_1}^L I_{R_f to L} \tilde{J}_{R_f}^{-1} \tilde{C}_{1,1}^{R_f} \left( I_{LtoR_f} R_L \mathbf{w}_L - R_f \mathbf{w}_{R_f} \right), \quad (61)$$

$$I_P^{R_f} \equiv - \left( P^{R_f} \right)^{-1} R_{R_f}^T P_{\perp \xi_1}^{R_f} \tilde{J}_{R_f}^{-1} \tilde{C}_{1,1}^{R_f} \left( R_{R_f} \mathbf{w}_{R_f} - I_{LtoR_f} R_L \mathbf{w}_L \right), \quad (62)$$

where

$$\tilde{C}_{1,1}^{R_f} \equiv \frac{1}{2} \left\{ \hat{C}_{1,1} \left( I_{LtoR_f} R_L \mathbf{q}_L \right) + \hat{C}_{1,1} \left( R_{R_f} \mathbf{q}_{R_f} \right) \right\},$$

and the diagonal matrix  $\tilde{J}_{R_f}$  has the metric Jacobian associated with surface of element  $R_f$  along its diagonal. The next theorem summarizes the properties of the viscous dissipation terms.

**Theorem 6** *The dissipation terms (61) and (62) are of order  $\min(p_L, p_{R_1}, \dots, p_{R_f}) + 3$ , lead to an entropy stable viscous scheme and have no impact on free-stream preservation.*

*Proof* The proofs are similar to those in Ref. [17] and are omitted for brevity.

In Section 7, four problems are used to characterize the  $h/p$  nonconforming algorithm: 1) the propagation of an isentropic vortex, 2) the propagation of a viscous shock, 3) the Taylor–Green vortex problem, and 4) the turbulent flow past a sphere. In all cases, the boundary conditions are weakly imposed by using the same type of mechanics as for the interface SATs discussed in this section (for details see [37, 14]).

## 7 Numerical experiments

In this section, we verify that the proposed  $h/p$ -algorithm retains the accuracy and robustness of the conforming algorithm [4,37,10].

The unstructured grid  $h/p$ -adaptive solver used herein has been developed at the Extreme Computing Research Center (ECRC) at KAUST on top of the Portable and Extensible Toolkit for Scientific computing (PETSc) [2], its mesh topology abstraction (DMPLEX) [30] and salable ordinary differential equation (ODE)/differential algebraic equations (DAE) solver library [1]. The  $p$ -refinement algorithm is fully implemented in the unstructured solver whereas the  $h$ -refinement strategy leverages the capabilities of the p4est library [3]. Additionally, the conforming numerical solver is based on the algorithms proposed in [4,37,10]. The systems of ODEs arising from the spatial discretizations are integrated using the fourth-order accurate Dormand–Prince method [22] endowed with an adaptive time stepping technique based on digital signal processing [41,42]. To make the temporal error negligible, a tolerance of  $10^{-8}$  is always used for the time-step adaptivity.

The errors are computed using volume scaled (for the  $L^1$  and  $L^2$  norms) discrete norms as follows:

$$\begin{aligned}\|\mathbf{u}\|_{L^1} &= \Omega_c^{-1} \sum_{\kappa=1}^K \mathbf{1}_{\kappa}^T \mathbf{P}^{\kappa} \mathbf{J}_{\kappa} \text{abs}(\mathbf{u}_{\kappa}), \\ \|\mathbf{u}\|_{L^2}^2 &= \Omega_c^{-1} \sum_{\kappa=1}^K \mathbf{u}_{\kappa}^T \mathbf{P}^{\kappa} \mathbf{J}_{\kappa} \mathbf{u}_{\kappa}, \\ \|\mathbf{u}\|_{L^{\infty}} &= \max_{\kappa=1\dots K} \text{abs}(\mathbf{u}_{\kappa}),\end{aligned}$$

where  $\Omega_c$  is the volume of  $\Omega$  computed as  $\Omega_c \equiv \sum_{\kappa=1}^K \mathbf{1}_{\kappa}^T \mathbf{P}^{\kappa} \mathbf{J}_{\kappa} \mathbf{1}_{\kappa}$ .

### 7.1 Isentropic Euler vortex propagation

For verification and characterization of the inviscid components of the algorithm, the propagation of an isentropic vortex is used. This benchmark problem has an analytical solution which is given by

$$\begin{aligned}\mathcal{G}(x_1, x_2, x_3, t) &= 1 - \left\{ [(x_1 - x_{1,0}) - U_{\infty} \cos(\alpha) t]^2 + [(x_2 - x_{2,0}) - U_{\infty} \sin(\alpha) t]^2 \right\}, \\ \rho &= T^{\frac{1}{\gamma-1}}, \\ \mathcal{U}_1 &= U_{\infty} \cos(\alpha) - \epsilon_{\nu} \frac{(x_2 - x_{2,0}) - U_{\infty} \sin(\alpha) t}{2\pi} \exp\left(\frac{\mathcal{G}}{2}\right), \\ \mathcal{U}_2 &= U_{\infty} \sin(\alpha) - \epsilon_{\nu} \frac{(x_1 - x_{1,0}) - U_{\infty} \cos(\alpha) t}{2\pi} \exp\left(\frac{\mathcal{G}}{2}\right), \\ \mathcal{U}_3 &= 0, \\ T &= \left[ 1 - \epsilon_{\nu}^2 M_{\infty}^2 \frac{\gamma-1}{8\pi^2} \exp(\mathcal{G}) \right],\end{aligned}$$

where  $U_\infty$ ,  $M_\infty$ , and  $(x_{1,0}, x_{2,0}, x_{3,0})$  are the modulus of the free-stream velocity, the free-stream Mach number, and the vortex center, respectively. In this paper, the following values are used:  $U_\infty = M_\infty c_\infty$ ,  $\epsilon_\nu = 5$ ,  $M_\infty = 0.5$ ,  $\gamma = 1.4$ ,  $\alpha = 45^\circ$ , and  $(x_{1,0}, x_{2,0}, x_{3,0}) = (0, 0, 0)$ . The computational domain is

$$x_1 \in [-5, 5], \quad x_2 \in [-5, 5], \quad x_3 \in [-5, 5], \quad t \in [0, 2].$$

The analytical solution is used to furnish data for the initial condition.

First, we report on the results aimed at validating the entropy conservation properties of the interior domain SBP-SAT algorithm. Thus, periodic boundary conditions are used on all six faces of the computational domain. Furthermore, all the dissipation terms used for the interface coupling are turned off. The discrete integral over the volume of the time rate of change of the entropy function,  $\int_\Omega \frac{\partial \mathcal{S}}{\partial t} d\Omega$ , is monitored at every time step. This means that at each time step the compressible Euler equations are multiplied by the discrete entropy variables to construct the discrete analog of the right-hand side of (51).

We subdivide the computational domain using ten hexahedrons in each coordinate direction. Subsequently, we split random cells in the mesh using one or two levels of  $h$ -refinement. Then, we assign the solution polynomial degree in each element to a random integer chosen uniformly from the set  $\{2, 3, 4, 5\}$  (i.e., each member in the set has an equal probability of being chosen). To test the conservation of entropy and therefore the free-stream condition when curved element interfaces are used we construct the the LGL collocation point coordinates at element interfaces<sup>1</sup> as follows:

- Construct a mesh using a  $p_i$ th-order polynomial approximation for the element interfaces.
- Perturb the nodes that are used to define the  $p_i$ th-order polynomial approximation of the element interfaces as follows:

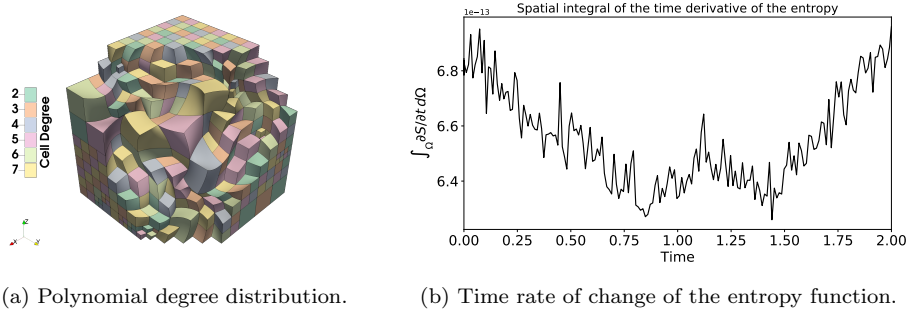
$$\begin{aligned} x_1 &= x_{1,*} + \frac{1}{15} L_1 \cos(a) \cos(3b) \sin(4c), \\ x_2 &= x_{2,*} + \frac{1}{15} L_2 \sin(4a) \cos(b) \cos(3c), \\ x_3 &= x_{3,*} + \frac{1}{15} L_3 \cos(3a) \sin(4b) \cos(c), \end{aligned}$$

where,

$$\begin{aligned} a &= \frac{\pi}{L_1} \left( x_{1,*} - \frac{x_{1,H} + x_{1,L}}{2} \right), \quad b = \frac{\pi}{L_2} \left( x_{2,*} - \frac{x_{2,H} + x_{2,L}}{2} \right), \\ c &= \frac{\pi}{L_3} \left( x_{3,*} - \frac{x_{3,H} + x_{3,L}}{2} \right). \end{aligned}$$

The symbols  $L_1$ ,  $L_2$  and  $L_3$  represent the dimensions of the computational domain in the three coordinate directions and the sub-script  $*$  indicates the unperturbed coordinate of the nodes. This step yields a perturbed  $p_i$ th-order polynomial.

<sup>1</sup> In a general setting, element interfaces can also be boundary element interfaces.



(a) Polynomial degree distribution. (b) Time rate of change of the entropy function.

Fig. 3: Isentropic Euler vortex.

- Compute the coordinate of the LGL points at the element interface by evaluating the perturbed  $p_i$ th-order polynomial at the LGL points used to define the cell solution polynomial of order  $p_s$ .

Herein, we use  $p_i = 2$ . Figure 3a shows a cut of the mesh where each cell is colored according to the solution polynomial degree assigned to it. Curved element interfaces are clearly visible.

The propagation of the vortex is simulated for two time units. Figure 3b plots the integral over the volume of the time derivative of the entropy function. We can see that the global variation of the discrete time rate of change of  $\mathcal{S}$  is practically zero (i.e., machine double precision). This implies that the nonconforming algorithm is entropy conservative.

Second, we perform a grid convergence study to investigate the order of convergence of the  $h/p$ -adaptive approach. The base grid (labeled with “0” in the first column of following tables) is constructed as follow:

- Divide the computational domain with four hexahedral elements in each coordinate direction.
- Refine random elements by using one or two levels of  $h$ -refinement.
- Assign the solution polynomial degree in each element to a random integer chosen uniformly from the set  $\{p_s, p_s + 1\}$ .
- Approximate the curved element interfaces with a  $p_s$ th-order accurate polynomial.
- Construct the perturbed elements and their corresponding LGL points as described previously.

From the base grid, which is similar to the one depicted in Figure 3a, a sequence of nested grids is then generated to perform the convergence study. The results are reported in Tables 1 through 4 for the error on the density. The number listed in the first column denoted by “Levels” indicates the number of uniform refinements in each coordinate direction.

For all the degree tested (i.e.  $p = 1$  to  $p = 5$ ), the order of convergence of the conforming and nonconforming algorithms is very similar. However, note that in the  $L^1$  and  $L^2$  norms the nonconforming algorithm is more accurate than the conforming one. In the discrete  $L^\infty$  norm, the nonconforming scheme is sometimes slightly worse than the conforming scheme; this most likely results from the fact that the interpolation matrices are sub-optimal.

Levels	Conforming, $p = 1$						Nonconforming, $p = 1$ and $p = 2$					
	$L^1$	Rate	$L^2$	Rate	$L^\infty$	Rate	$L^1$	Rate	$L^2$	Rate	$L^\infty$	Rate
0	2.74E-02	-	1.32E-03	-	1.55E-01	-	1.02E-02	-	5.80E-04	-	1.43E-01	-
1	1.14E-02	-1.26	6.61E-04	-1.00	1.12E-01	-0.47	4.38E-03	-1.22	2.82E-04	-1.04	7.17E-02	-1.00
2	5.13E-03	-1.16	3.31E-04	-1.00	7.29E-02	-0.62	1.45E-03	-1.60	9.99E-05	-1.50	4.30E-02	-0.74
3	1.70E-03	-1.59	1.15E-04	-1.52	3.01E-02	-1.28	4.16E-04	-1.80	3.02E-05	-1.72	2.29E-02	-0.91
4	4.76E-04	-1.84	3.24E-05	-1.83	8.53E-03	-1.82	1.11E-04	-1.91	8.76E-06	-1.79	1.06E-02	-1.10
5	1.23E-04	-1.96	8.33E-06	-1.96	2.13E-03	-2.00	2.61E-05	-2.09	2.28E-06	-1.94	4.05E-03	-1.40
6	3.08E-05	-1.99	2.09E-06	-1.99	5.24E-04	-2.02	6.31E-06	-2.05	5.75E-07	-1.99	1.25E-03	-1.70
7	7.68E-06	-2.00	5.23E-07	-2.00	1.30E-04	-2.01	1.56E-06	-2.02	1.50E-07	-1.94	4.45E-04	-1.48

Table 1: Convergence study of the isentropic vortex propagation: two levels of  $h$ -refinement,  $p = 1$  and  $p = 2$ ; density error.

Levels	Conforming, $p = 2$						Nonconforming, $p = 2$ and $p = 3$					
	$L^1$	Rate	$L^2$	Rate	$L^\infty$	Rate	$L^1$	Rate	$L^2$	Rate	$L^\infty$	Rate
0	9.75E-03	-	5.32E-04	-	1.24E-01	-	2.59E-03	-	1.75E-04	-	7.52E-02	-
1	3.18E-03	-1.61	2.09E-04	-1.35	6.97E-02	-0.83	4.11E-04	-2.65	3.45E-05	-2.34	3.14E-02	-1.26
2	5.18E-04	-2.62	3.88E-05	-2.43	2.51E-02	-1.47	4.91E-05	-3.07	5.13E-06	-2.75	8.16E-03	-1.95
3	6.38E-05	-3.02	5.50E-06	-2.82	7.23E-03	-1.79	5.86E-06	-3.07	6.74E-07	-2.93	2.09E-03	-1.97
4	7.61E-06	-3.07	7.23E-07	-2.93	1.21E-03	-2.58	7.05E-07	-3.06	8.97E-08	-2.91	4.32E-04	-2.27
5	9.48E-07	-3.00	9.95E-08	-2.86	2.75E-04	-2.14	8.54E-08	-3.04	1.20E-08	-2.91	1.00E-04	-2.11
6	1.23E-07	-2.94	1.43E-08	-2.83	3.41E-05	-3.01	9.98E-09	-3.10	1.56E-09	-2.94	2.52E-05	-1.99

Table 2: Convergence study of the isentropic vortex propagation: two levels of  $h$ -refinement,  $p = 2$  and  $p = 3$ ; density error.

Levels	Conforming, $p = 3$						Nonconforming, $p = 3$ and $p = 4$					
	$L^1$	Rate	$L^2$	Rate	$L^\infty$	Rate	$L^1$	Rate	$L^2$	Rate	$L^\infty$	Rate
0	5.22E-03	-	3.38E-04	-	9.16E-02	-	5.38E-04	-	4.51E-05	-	5.38E-02	-
1	6.84E-04	-2.93	5.30E-05	-2.67	4.71E-02	-0.96	4.18E-05	-3.69	3.89E-06	-3.54	5.42E-03	-3.31
2	5.50E-05	-3.64	4.54E-06	-3.55	6.61E-03	-2.83	2.61E-06	-4.00	2.82E-07	-3.78	6.47E-04	-3.07
3	3.48E-06	-3.98	3.33E-07	-3.77	5.47E-04	-3.59	1.79E-07	-3.86	1.92E-08	-3.88	7.36E-05	-3.14
4	2.10E-07	-4.05	2.45E-08	-3.76	4.93E-05	-3.47	1.09E-08	-4.04	1.23E-09	-3.96	6.93E-06	-3.41
5	1.39E-08	-3.92	1.87E-09	-3.71	6.32E-06	-2.96	7.05E-10	-3.96	8.10E-11	-3.93	8.10E-07	-3.10

Table 3: Convergence study of the isentropic vortex propagation: two levels of  $h$ -refinement,  $p = 3$  and  $p = 4$ ; density error.

## 7.2 Viscous shock propagation

Next we study the propagation of a viscous shock using the compressible Navier–Stokes equations. We assume a planar shock propagating along the  $x_1$  coordinate direction with a Prandtl number of  $Pr = 3/4$ . The exact solution of this problem

Levels	Conforming, $p = 4$						Nonconforming, $p = 4$ and $p = 5$					
	$L^1$	Rate	$L^2$	Rate	$L^\infty$	Rate	$L^1$	Rate	$L^2$	Rate	$L^\infty$	Rate
0	2.34E-03	-	1.56E-04	-	9.92E-02	-	7.48E-05	-	5.15E-06	-	4.21E-03	-
1	1.70E-04	-3.78	1.43E-05	-3.45	2.32E-02	-2.09	2.20E-06	-5.09	1.87E-07	-4.79	2.45E-04	-4.10
2	6.07E-06	-4.81	6.41E-07	-4.48	1.27E-03	-4.19	6.76E-08	-5.02	6.66E-09	-4.81	1.81E-05	-3.76
3	1.99E-07	-4.93	2.25E-08	-4.83	5.13E-05	-4.64	2.08E-09	-5.03	2.21E-10	-4.91	1.26E-06	-3.84
4	7.11E-09	-4.81	8.60E-10	-4.71	3.01E-06	-4.09	6.61E-11	-4.97	6.78E-12	-5.03	9.13E-08	-3.79

Table 4: Convergence study of the isentropic vortex propagation: two levels of  $h$ -refinement,  $p = 4$  and  $p = 5$ ; density error.

is known; the momentum  $\mathcal{V}(x_1)$  satisfies the ODE

$$\alpha \mathcal{V} \frac{\partial \mathcal{V}}{\partial x_1} - (\mathcal{V} - 1)(\mathcal{V} - \mathcal{V}_f) = 0; \quad -\infty \leq x_1 \leq +\infty, \quad t \geq 0, \quad (63)$$

whose solution can be written implicitly as

$$\begin{aligned} & x_1 - \frac{1}{2} \alpha (\log |(\mathcal{V}(x_1) - 1)(\mathcal{V}(x_1) - \mathcal{V}_f)| \\ & + \frac{1 + \mathcal{V}_f}{1 - \mathcal{V}_f} \log \left| \frac{\mathcal{V}(x_1) - 1}{\mathcal{V}(x_1) - \mathcal{V}_f} \right|) = 0, \end{aligned} \quad (64)$$

where

$$\mathcal{V}_f \equiv \frac{\mathcal{U}_L}{\mathcal{U}_R}, \quad \alpha \equiv \frac{2\gamma}{\gamma + 1} \frac{\mu}{Pr \mathcal{M}}. \quad (65)$$

Here  $\mathcal{U}_{L/R}$  are known velocities to the left and right of the shock at  $-\infty$  and  $+\infty$ , respectively,  $\mathcal{M}$  is the constant mass flow across the shock,  $Pr$  is the Prandtl number, and  $\mu$  is the dynamic viscosity. The mass and total enthalpy are constant across the shock. Moreover, the momentum and energy equations become redundant.

For our tests,  $\mathcal{V}$  is computed from Equation (64) to machine precision using bisection. The moving shock solution is obtained by applying a uniform translation to the above solution. The shock is located at the center of the domain at  $t = 0$  and the following values are used:  $M_\infty = 2.5$ ,  $Re_\infty = 10$ , and  $\gamma = 1.4$ . The domain is given by

$$x_1 \in [-0.5, 0.5], \quad x_2 \in [-0.5, 0.5], \quad x_3 \in [-0.5, 0.5], \quad t \in [0, 0.5].$$

The boundary conditions are prescribed by penalizing the numerical solution against the exact solution. The analytical solution is also used to furnish data for the initial condition.

The base grid (labeled with “0” in the first column of Tables 5 through 8) is constructed as described in Section 7.1. From the base grid, which is similar to the one depicted in Figure 3a, a sequence of nested grids is then generated to perform the convergence study. The results are reported in Tables 5 through 8 for the error on the density. Again, the number listed in the first column denoted by “Levels” indicates the number of uniform refinement in each coordinate direction.

Similar to the propagation of the inviscid vortex, for all the degree tested (i.e.,  $p = 1$  to  $p = 5$ ), the order of convergence of the conforming and nonconforming



algorithms is similar. However, note that, the nonconforming algorithm is more accurate than the conforming one, for all the three norms reported.

Levels	Conforming, $p = 1$						Nonconforming, $p = 1$ and $p = 2$					
	$L^1$	Rate	$L^2$	Rate	$L^\infty$	Rate	$L^1$	Rate	$L^2$	Rate	$L^\infty$	Rate
0	5.43E-02	-	6.54E-02	-	1.40E-01	-	1.31E-02	-	2.11E-02	-	7.32E-02	-
1	2.04E-02	-1.41	2.92E-02	-1.16	8.42E-02	-0.73	3.29E-03	-1.99	5.76E-03	-1.87	2.94E-02	-1.32
2	5.56E-03	-1.87	8.45E-03	-1.79	2.85E-02	-1.57	8.39E-04	-1.97	1.46E-03	-1.98	9.16E-03	-1.68
3	1.44E-03	-1.94	2.23E-03	-1.92	8.12E-03	-1.81	2.11E-04	-1.99	3.76E-04	-1.96	2.36E-03	-1.96
4	3.68E-04	-1.97	5.66E-04	-1.98	2.26E-03	-1.84	5.03E-05	-2.07	8.97E-05	-2.07	5.97E-04	-1.98
5	9.28E-05	-1.99	1.43E-04	-1.99	6.05E-04	-1.90	1.24E-05	-2.02	2.10E-05	-2.09	1.48E-04	-2.01

Table 5: Convergence study of the viscous shock propagation: two levels of  $h$ -refinement,  $p = 1$  and  $p = 2$ ; density error.

Levels	Conforming, $p = 2$						Nonconforming, $p = 2$ and $p = 3$					
	$L^1$	Rate	$L^2$	Rate	$L^\infty$	Rate	$L^1$	Rate	$L^2$	Rate	$L^\infty$	Rate
0	1.78E-02	-	2.68E-02	-	1.36E-01	-	1.85E-03	-	3.84E-03	-	4.86E-02	-
1	2.93E-03	-2.60	5.05E-03	-2.41	5.98E-02	-1.19	2.75E-04	-2.75	5.85E-04	-2.72	1.11E-02	-2.14
2	3.86E-04	-2.92	6.93E-04	-2.87	1.09E-02	-2.45	4.01E-05	-2.78	8.74E-05	-2.74	2.03E-03	-2.45
3	5.55E-05	-2.80	1.03E-04	-2.74	2.23E-03	-2.29	5.00E-06	-3.00	1.01E-05	-3.11	3.18E-04	-2.67
4	8.96E-06	-2.63	1.79E-05	-2.53	4.96E-04	-2.17	6.10E-07	-3.04	1.23E-06	-3.04	4.20E-05	-2.92
5	1.46E-06	-2.66	2.99E-06	-2.58	8.96E-05	-2.47	7.00E-08	-3.12	1.51E-07	-3.03	5.50E-06	-2.93

Table 6: Convergence study of the viscous shock propagation: two levels of  $h$ -refinement,  $p = 2$  and  $p = 3$ ; density error.

Levels	Conforming, $p = 3$						Nonconforming, $p = 3$ and $p = 4$					
	$L^1$	Rate	$L^2$	Rate	$L^\infty$	Rate	$L^1$	Rate	$L^2$	Rate	$L^\infty$	Rate
0	4.45E-03	-	7.52E-03	-	7.51E-02	-	2.41E-04	-	5.24E-04	-	1.12E-02	-
1	3.40E-04	-3.71	6.50E-04	-3.53	1.19E-02	-2.66	1.80E-05	-3.74	4.11E-05	-3.67	1.01E-03	-3.47
2	2.67E-05	-3.67	5.36E-05	-3.60	1.20E-03	-3.30	1.21E-06	-3.90	3.00E-06	-3.78	8.17E-05	-3.63
3	1.95E-06	-3.77	4.25E-06	-3.66	1.25E-04	-3.26	7.30E-08	-4.05	1.90E-07	-3.98	5.82E-06	-3.81
4	1.48E-07	-3.72	3.67E-07	-3.53	1.12E-05	-3.48	4.23E-09	-4.11	1.09E-08	-4.13	3.60E-07	-4.02

Table 7: Convergence study of the viscous shock propagation: two levels of  $h$ -refinement,  $p = 3$  and  $p = 4$ ; density error.

Levels	Conforming, $p = 4$						Nonconforming, $p = 4$ and $p = 5$					
	$L^1$	Rate	$L^2$	Rate	$L^\infty$	Rate	$L^1$	Rate	$L^2$	Rate	$L^\infty$	Rate
0	1.21E-03	-	2.28E-03	-	2.50E-02	-	3.47E-05	-	8.15E-05	-	1.90E-03	-
1	8.50E-05	-3.83	1.54E-04	-3.88	3.04E-03	-3.04	1.37E-06	-4.66	3.13E-06	-4.70	8.02E-05	-4.57
2	2.75E-05	-4.95	5.66E-06	-4.77	1.52E-04	-4.32	4.73E-08	-4.85	1.10E-07	-4.83	3.04E-06	-4.72
3	1.16E-07	-4.57	2.54E-07	-4.48	7.54E-06	-4.33	1.62E-09	-4.87	3.62E-09	-4.93	1.44E-07	-4.40
4	5.21E-09	-4.48	1.11E-08	-4.52	4.01E-07	-4.23	6.01E-11	-4.75	1.30E-10	-4.80	6.96E-09	-4.37

Table 8: Convergence study of the viscous shock propagation: two levels of  $h$ -refinement,  $p = 4$  and  $p = 5$ ; density error.

### 7.3 Taylor–Green vortex at $Re = 1,600$

The purpose of this section is to demonstrate that the nonconforming algorithm has the same stability properties as the conforming algorithm. To do so, the Taylor–Green vortex problem on a very coarse grid is solved.

The numerical solution is computed in a periodic cube  $[-\pi L \leq x, y, z \leq \pi L]$  and the initial condition is given by

$$\begin{aligned}
\mathcal{U}_1 &= \mathcal{V}_0 \sin\left(\frac{x_1}{L}\right) \cos\left(\frac{x_2}{L}\right) \cos\left(\frac{x_3}{L}\right), \\
\mathcal{U}_2 &= -\mathcal{V}_0 \cos\left(\frac{x_1}{L}\right) \sin\left(\frac{x_2}{L}\right) \cos\left(\frac{x_3}{L}\right), \\
\mathcal{U}_3 &= 0, \\
\mathcal{P} &= \mathcal{P}_0 + \frac{\rho_0 \mathcal{V}_0^2}{16} \left[ \cos\left(\frac{2x_1}{L}\right) + \cos\left(\frac{2x_2}{L}\right) \right] \left[ \cos\left(\frac{2x_3}{L} + 2\right) \right].
\end{aligned} \tag{66}$$

The flow is initialized to be isothermal, i.e.,  $\mathcal{P}/\rho = \mathcal{P}_0/\rho_0 = R\mathcal{T}_0$ , and  $\mathcal{P}_0 = 1$ ,  $\mathcal{T}_0 = 1$ ,  $L = 1$ , and  $\mathcal{V}_0 = 1$ . Finally, the Reynolds number is defined by  $Re = (\rho_0 \mathcal{V}_0)/\mu$ , where  $\mu$  is the dynamic viscosity.

In order to obtain results that are reasonably close to those found for the incompressible equations, a Mach number of  $M = 0.05$  is used. Furthermore, the Reynolds number, the Prandtl number, and the initial density distribution are set to  $Re = 1,600$ ,  $Pr = 0.71$ , and  $\rho_0 = \gamma M^2$ , respectively, where  $\gamma = 1.4$ .

For this test case, a grid is constructed as follow:

- Divide the computational domain with  $N_{1h}$  hexahedral elements in each coordinate direction.
- Refine random elements by using randomly one or two levels of  $h$ -refinement.
- Assign the solution polynomial degree in each element to a random integer chosen uniformly from a set (see the legend in Figure 4).
- Construct the perturbed elements and their corresponding LGL points as described previously (the element interfaces are approximated using a polynomial degree which is the minimum solution polynomial degree used in the simulation).

Herein, two grids with  $N_{1h} = 4$  and  $N_{1h} = 8$  are considered. Their total number of hexahedrons is 869 and 7547, respectively. The simulations are run without additional stabilization mechanisms (dissipation model, de-aliasing, filtering, etc.),

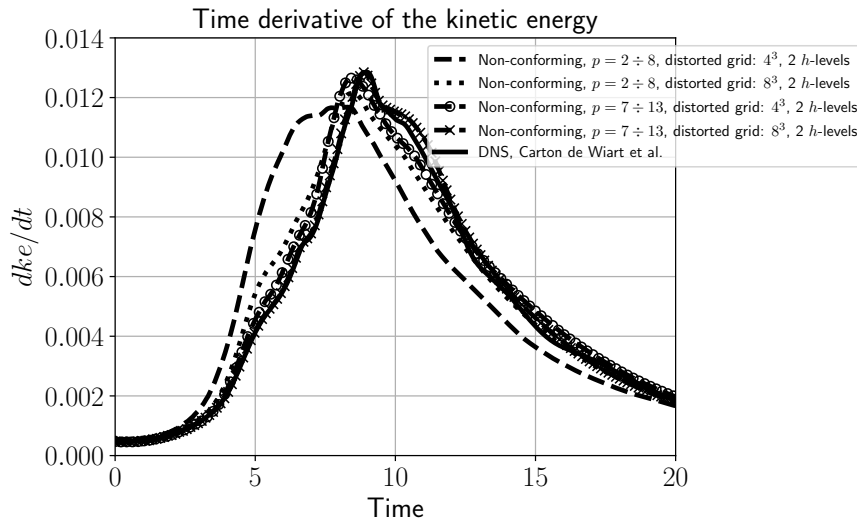


Fig. 4: Evolution of the time derivative of the kinetic energy for the Taylor–Green vortex at  $Re = 1,600$ ,  $M = 0.05$ .

where the only numerical dissipation originates from the upwind inter-element coupling procedure.

Figure 4 shows the time rate of change of the kinetic energy,  $dke/dt$ , for the nonconforming algorithm using a random distribution of solution polynomial order between i)  $p = 2$  and  $p = 8$  and ii)  $p = 7$  and  $p = 13$ . The reference DNS solution reported in [51] is also plotted. We note that by increasing the order of accuracy of the solution polynomial in each cell and the grid density the solution get closer to the DNS solution. The main take-away from the figure is that all simulations are stable, which is numerical evidence that the  $h/p$  nonconforming scheme inherits the stability characteristics of the conforming and fully-staggered algorithms [4, 37, 5, 10, 35].

#### 7.4 Flow around a sphere at $Re = 2,000$

In this section, we test our implementation within a more complex setting represented by the flow around a sphere at  $Re = 2,000$  and  $M = 0.05$ . With this value of the Reynolds number the flow is fully turbulent. In this case, a sphere of diameter  $d$  is centered at the origin of the axes, and a box is respectively extended  $20d$  and  $60d$  upstream and downstream the direction of the flow; the box size is  $30d$  in both the  $x_2$  and  $x_3$  directions. As boundary conditions, we consider adiabatic solid walls at the surface of the sphere [14] and far field on all faces of the box. We use a grid with 24,704 hexahedral elements. Figure 5 shows the mesh near the sphere. The colors indicates the solution polynomial order used in each cell. The quality of the elements is good in the boundary layer region whereas in the other portion of the domain is fairly poor. This choice is intentional and is for the purpose of demonstrating the performance of the algorithm on non-ideal grids.

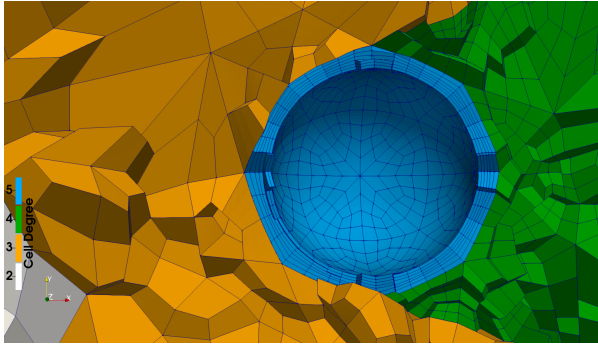


Fig. 5: Polynomial degree distribution for the mesh around a sphere.

	$\langle C_D \rangle$
Munson et al. [31]	0.412
Present	0.416

Table 9: Time-average drag coefficient of a sphere at  $Re = 2,000$ ,  $M = 0.05$ .

We compute the time-average value of the drag coefficient,  $\langle C_D \rangle$ , and we compare it with the value reported in literature [31]. From Table 9, it can be seen that the computed time-average drag coefficient matches very well the value reported in literature.

### 7.5 Entropy conservation of the fully-discrete explicit discretization

To conclude the numerical results section, we demonstrate the entropy conservation of the fully-discrete explicit discretization of the compressible Navier–Stokes equations by integrating in time the system of ODEs which arise from the spatial discretization with an explicit relaxation Runge–Kutta scheme [38]. As shown in [29, 38], the term “relaxation” represents a general approach which allows any Runge–Kutta method to preserve the correct time evolution of an arbitrary functional, without sacrificing the linear covariance, accuracy, or stability properties of the original method. In the context of the compressible Euler and Navier–Stokes equations, the relaxation Runge–Kutta scheme is constructed to preserve the discrete entropy function obtained from the spatial discretization. This leads to a fully discrete algorithm which is entropy conservative or entropy stable if the spatial discretization is entropy conservative or entropy stable, respectively.

As a model problem, we again use the propagation of an isentropic vortex and we analyze the time evolution of the entropy function, which for the current setting must be zero. The same grid and solution polynomial distribution shown in Figure 3a is used for this test case. To achieve entropy conservation at the spatial level, all the dissipation terms used for the interface coupling are turned off, including upwind and interior penalty SATs. The fourth-order accurate Dormand–Prince method [22] with and without relaxation algorithm are used. We show the entropy variation in Figure 6. The entropy is conserved up to machine (double) preci-

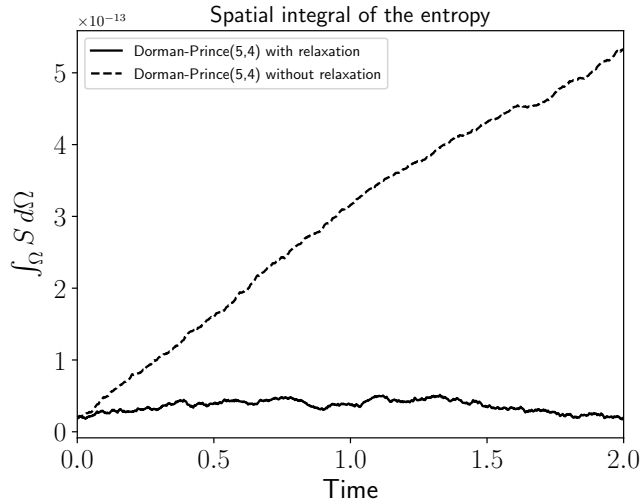


Fig. 6: Evolution of the discrete spatial integral of the entropy function.

sion using relaxation, whereas, without relaxation, the solution shows significant essentially monotone changes in total entropy function.

## 8 Conclusions

In this paper, the  $p$ -refinement/coarsening algorithms in [17,18,16] are extended to arbitrary  $h/p$ -refinement/coarsening. In order to obtain an algorithm for which the discrete GCL conditions are solved for element by element, the surface metric terms need to be localized to the small elements on an  $h$ -refined face. The discrete GCL conditions are then solved using the procedure in Crean *et al.* [12]. The resulting algorithm is entropy conservative/stable, element-wise conservative, and free-stream preserving. Finally, the algorithm is shown to retain the accuracy and stability characteristics of the original conforming scheme on a set of test problems and, when coupled with relaxation Runge–Kutta schemes [38], yields a fully discrete entropy conservative/stable scheme.

**Acknowledgements** The research reported in this publication was supported by funding from King Abdullah University of Science and Technology (KAUST). We are thankful for the computing resources of the Supercomputing Laboratory and the Extreme Computing Research Center at KAUST. Special thanks are extended to Dr. Mujeeb R. Malik for supporting this work as part of NASA’s “Transformational Tools and Technologies” ( $T^3$ ) project.

## References

1. Abhyankar, S., Brown, J., Constantinescu, E.M., Ghosh, D., Smith, B.F., Zhang, H.: PETSc/TS: A modern scalable ODE/DAE solver library. arXiv preprint arXiv:1806.01437 (2018)

2. Balay, S., Abhyankar, S., Adams, M.F., Brown, J., Brune, P., Buschelman, K., Dalcin, L., Dener, A., Eijkhout, V., Gropp, W.D., Karpeyev, D., Kaushik, D., Knepley, M.G., May, D.A., McInnes, L.C., Mills, R.T., Munson, T., Rupp, K., Sanan, P., Smith, B.F., Zampini, S., Zhang, H., Zhang, H.: PETSc users manual. Tech. Rep. ANL-95/11 - Revision 3.11, Argonne National Laboratory (2019)
3. Burstedde, C., Wilcox, L.C., Ghattas, O.: **p4est**: Scalable algorithms for parallel adaptive mesh refinement on forests of octrees. *SIAM Journal on Scientific Computing* **33**(3), 1103–1133 (2011). DOI 10.1137/100791634
4. Carpenter, M.H., Fisher, T.C., Nielsen, E.J., Frankel, S.H.: Entropy stable spectral collocation schemes for the Navier–Stokes equations: discontinuous interfaces. *SIAM Journal on Scientific Computing* **36**(5), B835–B867 (2014)
5. Carpenter, M.H., Fisher, T.C., Nielsen, E.J., Parsani, M., Svärd, M., Yamaleev, N.: Entropy stable summation-by-parts formulations for computational fluid dynamics. *Handbook of Numerical Analysis* (17), 495–524 (2016)
6. Carpenter, M.H., Gottlieb, D., Abarbanel, S.: Time-stable boundary conditions for finite-difference schemes solving hyperbolic systems: Methodology and application to high-order compact schemes. *Journal of Computational Physics* **111**(2), 220–236 (1994)
7. Carpenter, M.H., Nordström, J., Gottlieb, D.: A stable and conservative interface treatment of arbitrary spatial accuracy. *Journal of Computational Physics* **148**(2), 341–365 (1999)
8. Carpenter, M.H., Nordström, J., Gottlieb, D.: Revisiting and extending interface penalties for multi-domain summation-by-parts operators. *Journal of Scientific Computing* **45**(1-3), 118–150 (2010)
9. Carpenter, M.H., Parsani, M., Fisher, T.C., Nielsen, E.J.: Entropy stable staggered grid spectral collocation for the Burgers’ and compressible Navier–Stokes equations. NASA TM-2015-218990 (2015)
10. Carpenter, M.H., Parsani, M., Fisher, T.C., Nielsen, E.J.: Towards an entropy stable spectral element framework for computational fluid dynamics. In: 54th AIAA Aerospace Sciences Meeting, AIAA 2016-1058. American Institute of Aeronautics and Astronautics (AIAA) (2016)
11. Chan, J., Del Rey Fernández, D.C., Carpenter, M.H.: Efficient entropy stable Gauss collocation methods. (Submitted to *SIAM Journal on Scientific Computing*) (2018)
12. Crean, J., Hicken, J.E., Del Rey Fernández, D.C., Zingg, D.W., Carpenter, M.H.: Entropy-stable summation-by-parts discretization of the Euler equations on general curved elements. *Journal of Computational Physics* **356**, 410–438 (2018)
13. Dafermos, C.M.: *Hyperbolic conservation laws in continuum physics*. Springer-Verlag, Berlin (2010)
14. Dalcin, L., Rojas, D., Zampini, S., Del Rey Fernández, D.C., Carpenter, M.H., Parsani, M.: Conservative and entropy stable solid wall boundary conditions for the compressible Navier–Stokes equations: Adiabatic wall and heat entropy transfer. *Journal of Computational Physics* **397** (2019)
15. Del Rey Fernández, D.C., Boom, P.D., Zingg, D.W.: A generalized framework for nodal first derivative summation-by-parts operators. *Journal of Computational Physics* **266**(1), 214–239 (2014)
16. Del Rey Fernández, D.C., Carpenter, M.H., Dalcin, L., Fredrich, L., Winters, A.R., Gassner, G.J., Zampini, S., Parsani, M.: Entropy stable non-conforming discretizations with the summation-by-parts property for curvilinear coordinates. NASA TM-2019- (2019)
17. Del Rey Fernández, D.C., Carpenter, M.H., Dalcin, L., Fredrich, L., Winters, A.R., Gassner, G.J., Zampini, S., Parsani, M.: Entropy stable nonconforming discretization with the summation-by-parts property for the compressible Navier–Stokes equations. *Submitted Computers & fluids* (2019)
18. Del Rey Fernández, D.C., Carpenter, M.H., Dalcin, L., Fredrich, L., Winters, A.R., Gassner, G.J., Zampini, S., Parsani, M.: Entropy stable  $p$ -nonconforming discretizations with the summation-by-parts property for the compressible Euler equations. *Submitted SIAM Journal of Scientific Computing* (2019)
19. Del Rey Fernández, D.C., Crean, J., Carpenter, M.H., Hicken, J.E.: Staggered entropy-stable summation-by-parts discretization of the Euler equations on general curved elements. *Journal of Computational Physics* **392**, 161–186 (2019)
20. Del Rey Fernández, D.C., Hicken, J.E., Zingg, D.W.: Review of summation-by-parts operators with simultaneous approximation terms for the numerical solution of partial differential equations. *Computers & Fluids* **95**(22), 171–196 (2014)

21. Derigs, D., Winters, A.R., J.Gassner, G., Walch, S.: A novel averaging technique for discrete entropy-stable dissipation operators for ideal MHD. *Journal of Computational Physics* **330**(1), 624–632 (2017)
22. Dormand, J.R., Prince, P.J.: A family of embedded Runge–Kutta formulae. *Journal of Computational and Applied Mathematics* **6**(1), 19 – 26 (1980)
23. Fisher, T.C.: High-order  $l^2$  stable multi-domain finite difference method for compressible flows. Ph.D. thesis, Purdue University (2012)
24. Fisher, T.C., Carpenter, M.H.: High-order entropy stable finite difference schemes for nonlinear conservation laws: Finite domains. *Journal of Computational Physics* **252**(1), 518–557 (2013)
25. Fisher, T.C., Carpenter, M.H., Nordström, J., Yamaleev, N.K.: Discretely conservative finite-difference formulations for nonlinear conservation laws in split form: Theory and boundary conditions. *Journal of Computational Physics* **234**(1), 353–375 (2013)
26. Friedrich, L., Shnücke, G., Winters, A.R., Del Rey Fernández, D.C., Gassner, G.J., Carpenter, M.H.: Entropy stable space-time discontinuous Galerkin schemes with summation-by-parts property for hyperbolic conservation laws. *Journal of Scientific Computing* **80**(1), 175–222 (2019)
27. Friedrich, L., Winters, A.R., Del Rey Fernández, D.C., Gassner, G.J., Parsani, M., Carpenter, M.H.: An entropy stable  $h/p$  non-conforming discontinuous Galerkin method with the summation-by-parts property. *Journal of Scientific Computing* pp. 1–37 (2018)
28. Gassner, G.J., Winters, A.R., Kopriva, D.A.: A well balanced and entropy conservative discontinuous Galerkin spectral element method for the shallow water equations. *Applied Mathematics and Computation* **272**(2), 291–308 (2016)
29. Ketcheson, D.I.: Relaxation Runge–Kutta methods: Conservation and stability for inner-product norms (2019)
30. Knepley, M.G., Karpeev, D.A.: Mesh algorithms for PDE with Sieve I: Mesh distribution. *Scientific Programming* **17**(3), 215–230 (2009)
31. Munson, B.R., Young, B.F., Okiishi, T.H.: *Fundamental of fluid mechanics*, second edn. Wiley (1990)
32. Nordström, J., Carpenter, M.H.: Boundary and interface conditions for high-order finite-difference methods applied to the Euler and Navier–Stokes equations. *Journal of Computational Physics* **148**(2), 621–645 (1999)
33. Nordström, J., Carpenter, M.H.: High-order finite-difference methods, multidimensional linear problems, and curvilinear coordinates. *Journal of Computational Physics* **173**(1), 149–174 (2001)
34. Olsson, P., Olinger, J.: Energy and maximum norm estimates for nonlinear conservation laws. Tech. Rep. 94–01, The Research Institute of Advanced Computer Science (1994)
35. Parsani, M., Carpenter, M.H., Fisher, T.C., Nielsen, E.J.: Entropy stable staggered grid discontinuous spectral collocation methods of any order for the compressible Navier–Stokes equations. *SIAM Journal on Scientific Computing* **38**(5), A3129–A3162 (2016)
36. Parsani, M., Carpenter, M.H., Nielsen, E.J.: Entropy stable discontinuous interfaces coupling for the three-dimensional compressible Navier–Stokes equations. *Journal of Computational Physics* **290**, 132–138 (2015)
37. Parsani, M., Carpenter, M.H., Nielsen, E.J.: Entropy stable wall boundary conditions for the three-dimensional compressible Navier–Stokes equations. *Journal of Computational Physics* **292**(1), 88–113 (2015)
38. Ranocha, H., Sayyari, M., Dalcin, L., Parsani, M., Ketcheson, D.I.: Relaxation Runge–Kutta methods: Fully-discrete explicit entropy-stable schemes for the Euler and Navier–Stokes equations (2019). Submitted to *SIAM Journal on Scientific Computing*
39. Sandham, N.D., Li, Q., Yee, H.C.: Entropy splitting for high-order numerical simulation of compressible turbulence. *Journal of Computational Physics* **178**(2), 307–322 (2002)
40. Sjörn, B., Yee, H.C.: High order entropy conservative central schemes for wide ranges of compressible gas dynamics and MHD flows. *Journal of Computational Physics* **364**, 153–185 (2018)
41. Söderlind, G.: Digital filters in adaptive time-stepping. *ACM Transactions on Mathematical Software* **29**(1), 1–26 (2003)
42. Söderlind, G., Wang, L.: Adaptive time-stepping and computational stability. *Journal of Computational and Applied Mathematics* **185**(2), 225–243 (2006)
43. Svärd, M.: Weak solutions and convergent numerical schemes of modified compressible Navier–Stokes equations. *Journal of Computational Physics* **288**(C), 19–51 (2015)

44. Svärd, M., Carpenter, M.H., Parsani, M.: Entropy stability and the no-slip wall boundary condition. *SIAM Journal on Numerical Analysis* **56**(1), 256–273 (2018)
45. Svärd, M., Nordström, J.: Review of summation-by-parts schemes for initial-boundary-value-problems. *Journal of Computational Physics* **268**(1), 17–38 (2014)
46. Svärd, M., Özcan, H.: Entropy-stable schemes for the Euler equations with far-field and wall boundary conditions. *Journal of Scientific Computing* **58**(1), 61–89 (2014)
47. Tadmor, E.: The numerical viscosity of entropy stable schemes for systems of conservation laws I. *Mathematics of Computation* **49**(179), 91–103 (1987)
48. Tadmor, E.: Entropy stability theory for difference approximations of nonlinear conservation laws and related time-dependent problems. *Acta Numerica* **12**, 451–512 (2003)
49. Thomas, D., Lombard, C.K.: Geometric conservation law and its application to flow computations on moving grids. *AIAA Journal* **17**(10), 1030–1037 (1979)
50. Vinokur, M., Yee, H.C.: Extension of efficient low dissipation high order schemes for 3-d curvilinear moving grids. In: D.A. Caughey, M. Hafez (eds.) *Frontiers of Computational Fluid Dynamics*, pp. 129–164. World Scientific Publishing Company (2002)
51. de Wiart, C., Hillewaert, K., Duponcheel, M., Winckelmans, G.: Assessment of a discontinuous Galerkin method for the simulation of vortical flows at high Reynolds number. *International Journal for Numerical Methods in Fluids* **74**(7), 469–493 (2014)
52. Wintermeyer, N., Winters, A.R., Gassner, G.J., Kopriva, D.A.: An entropy stable nodal discontinuous Galerkin method for the two dimensional shallow water equations on unstructured curvilinear meshes with discontinuous bathymetry. *Journal of Computational Physics* **340**(1), 200–242 (2017)
53. Winters, A.R., Derigs, D., Gassner, G.J., Walch, S.: Uniquely defined entropy stable matrix dissipation operator for high Mach number ideal MHD and compressible Euler simulations. *Journal of Computational Physics* **332**(1), 274–289 (2017)
54. Winters, A.R., J.Gassner, G.: A comparison of two entropy stable discontinuous Galerkin spectral element approximations to the shallow water equations with non-constant topography. *Journal of Computational Physics* **301**(1), 357–376 (2015)
55. Yamaleev, N.K., Carpenter, M.H.: A family of fourth-order entropy stable non-oscillatory spectral collocation schemes for the 1-d Navier-Stokes equations. *Journal of Computational Physics* **331**, 90–107 (2017)
56. Yee, H.C., Vinokur, M., Djomehri, M.J.: Entropy splitting and numerical dissipation. *Journal of Computational Physics* **162**(1), 33–81 (2000)